*Electronic Research Archive*

https://www.aimspress.com/journal/era

ERA, 34(2): 1124–1156.
DOI: 10.3934/era.2026052
Received: 27 November 2025
Revised: 17 January 2026
Accepted: 27 January 2026
Published: 05 February 2026

*Research article*

# Meshless collocation methods for time-dependent nonlocal problems based on radial basis functions

**Qiao Zhuang**[1,*], **Yanzhi Zhang**[2] **and Zhongqiang Zhang**[3]

[1] School of Science and Engineering, University of Missouri-Kansas City, Kansas City, MO 64110, USA

[2] Department of Mathematics and Statistics, Missouri University of Science and Technology, Rolla, MO 65409, USA

[3] Department of Mathematical Sciences, Worcester Polytechnic Institute, Worcester, MA 01609, USA

* **Correspondence:** Email: qzhuang@umkc.edu.

**Abstract:** We present radial basis function (RBF) collocation methods for time-dependent space-fractional problems on general bounded domains. Building on a recently developed approach for accurately computing the integral fractional Laplacian of any RBF, we design collocation schemes for fractional heat and Stokes equations using extended-domain techniques. In particular, we propose a numerical Leray projection method for fractional Stokes problems, where both the discrete projection operator and the collocation scheme are formulated on extended domains to handle complex domains. Numerical results demonstrate the effectiveness of the proposed methods in solving time-dependent nonlocal problems on complex domains.

**Keywords:** meshless collocation methods; time-dependent nonlocal problems; fractional heat equation; fractional Stokes equation; radial basis functions

## 1. Introduction

In this paper, we develop collocation methods based on radial basis functions (RBFs) for time-dependent space-fractional problems, specifically addressing the fractional heat problem in (2.1)–(2.3) and the fractional Stokes problem in (3.1)–(3.4).

### 1.1. Significance of time-dependent space-fractional models

Space-fractional models are powerful tools for describing complex phenomena with long-range interactions and spatial heterogeneity; when combined with a temporal derivative, the resulting time-dependent models capture not only spatial complexity but also the transient dynamics of the system. Examples include fractional reaction–diffusion equations for modeling transport in porous media [1], as well as fractional heat equations for anomalous heat conduction [2, 3], such as those describing heat transfer dynamics in hybrid nanofluids [3]. In particular, the fractional heat equation serves as a prototype time-dependent extension of fractional elliptic models, where the temporal evolution highlights important aspects such as stability and long-time behavior, thus providing a fundamental testbed before addressing more complex fractional systems.

Moving from these scalar transport models to fluid motion, a particularly notable example is the fractional Navier–Stokes equations (NSE), which describe turbulent flows [4, 5] and can be derived from Boltzmann kinetic theory [5]. The linear counterpart of fractional NSE–fractional Stokes equations, which describe slow and viscous-dominated flows, provides a natural starting point for understanding the fractional NSE. By removing the nonlinear advection term, the model allows the study to focus on the effects of nonlocal diffusion and long-range spatial interactions. This simplification facilitates kinetic-theory-based modeling [6], enables theoretical analysis such as well-posedness of the weak formulation [7], and offers a more reliable baseline for validating numerical methods previously designed for fractional NSE, which underscores the significance of studying fractional Stokes problems.

### 1.2. Literature on numerical methods for time-dependent space-fractional problems

Various numerical methods have been developed to solve time-dependent space-fractional problems, including finite difference methods [8, 9], finite element methods [1, 10], and spectral methods [11, 12], just to name a few. These approaches are mesh-based or rely on structured collocation point distributions.

An alternative to mesh-based approaches is the use of meshless radial basis function methods, which offer greater flexibility in accommodating complex domains. Among many meshless RBF methods, those formulated in a pseudo-spectral framework are of particular interest because this framework is structurally compatible with nonlocal operators and allows for efficient implementation. This class of methods has been developed for space-fractional elliptic problems [13–16], as well as for time-dependent heat and wave equations [14, 15]. However, to our best knowledge, their application to fractional Stokes problems remains unexplored. We also refer readers to related RBF methods that incorporate specialized treatments, such as RBF-differential quadrature techniques [17, 18], which approximate space-fractional derivatives with weighted linear combinations of function values at scattered nodes.

In practice, RBF methods may suffer from ill-conditioning, particularly when Gaussian kernels with small shape parameters are used [19–21]; see also [22] and the references therein for results on conditioning and preconditioning from a numerical linear algebra perspective. To address this, RBF-QR methods [19, 20] were developed based on a change-of-basis technique, modifying the RBF basis functions to enhance linear independence while preserving the original function space. This approach has been successfully applied to space-fractional problems [21, 23]. In addition to

RBF-QR, other strategies, such as collocation methods based on extended domains in our previous work [24], can also improve conditioning and enhance numerical stability, which we briefly review in the following subsection.

### *1.3. Closely related works*

For fractional problems, the numerical stability is not only affected by the conditioning but also by the singularity of the integral fractional Laplacian. To illustrate this, we consider the following fractional Poisson problem:

$$(-\Delta)^{\gamma/2}u(\mathbf{x}) = f(\mathbf{x}), \quad \mathbf{x} \in \Omega \subset \mathbb{R}^d, \tag{1.1}$$

$$u(\mathbf{x}) = g(\mathbf{x}), \quad \mathbf{x} \in \Omega^c = \mathbb{R}^d \setminus \Omega. \tag{1.2}$$

Recall the definition of the fractional Laplacian [25–27]

$$(-\Delta)^{\frac{\gamma}{2}}u(\mathbf{x}) = c_{d,\gamma}\,\text{P.V.}\int_{\mathbb{R}^d}\frac{u(\mathbf{x})-u(\mathbf{y})}{|\mathbf{x}-\mathbf{y}|^{d+\gamma}}\,d\mathbf{y}, \quad \text{for } \gamma \in (0,2), \tag{1.3}$$

where $d$ indicates the spatial dimension, P.V. stands for the Cauchy principal value, and $c_{d,\gamma}$ represents the normalization constant. Denote an RBF approximation of the solution of the problems (1.1) and (1.2) as $\hat{u}$, and then using the definition in (1.3), the fractional Laplacian in (1.1) can be approximated by [14]

$$(-\Delta)_h^{\gamma/2}\hat{u}(\mathbf{x}) = (-\Delta)^{\gamma/2}\hat{u}(\mathbf{x}) + \mathcal{A}\hat{u}, \quad \mathcal{A}u = c_{d,\gamma}\int_{\Omega^c}\frac{u(\mathbf{y})-g(\mathbf{y})}{|\mathbf{x}-\mathbf{y}|^{d+\gamma}}\,d\mathbf{y}. \tag{1.4}$$

Based on (1.4), the RBF collocation scheme for the fractional Poisson problem was designed in [14], which deployed the collocation points in the interior domain $\Omega$ and on the boundary. We note that the exterior integral $\mathcal{A}\hat{u}$ term in (1.4) may introduce a weak singularity under the computational sense (i.e., produce large values), when $\mathbf{x}$ is close to the boundary. To mitigate this issue, our previous work [24] introduced the extended domain $\widetilde{\Omega}$ and redesigned (1.4) into the following form:

$$(-\Delta)_h^{\gamma/2}\hat{u}(\mathbf{x}) = (-\Delta)^{\gamma/2}\hat{u}(\mathbf{x}) + \mathcal{B}\hat{u}, \quad \mathcal{B}u = c_{d,\gamma}\int_{\widetilde{\Omega}^c}\frac{u(\mathbf{y})-g(\mathbf{y})}{|\mathbf{x}-\mathbf{y}|^{d+\gamma}}\,d\mathbf{y}. \tag{1.5}$$

This design mitigates the weak singularity (under the computational sense) and numerically demonstrates its capability in improving conditioning [24]. Compared to [14], this approach also collocates in $\widetilde{\Omega} \setminus \Omega$, in addition to $\Omega$ and $\partial\Omega$.

To deliver RBF collocation methods for nonlocal problems, a crucial component is effectively computing the integral fractional Laplacian of an RBF kernel $\phi(|\cdot|)$, i.e., $(-\Delta)^{\gamma/2}\phi$. Indeed, using the Hankel transform and the fact that $(-\Delta)^{\gamma/2}v = \mathcal{F}^{-1}(|\xi|^{\gamma}(\mathcal{F}v)(\xi))$, one can obtain

$$(-\Delta)^{\gamma/2}\phi(r) = r^{1-\frac{d}{2}}\int_0^{\infty}\omega^{\frac{d}{2}+\gamma}(\mathcal{F}\phi)(\omega)J_{\frac{d}{2}-1}(\omega r)\,d\omega, \tag{1.6}$$

where $\mathcal{F}$ is the Fourier transform, and $J_\nu(\cdot)$ Bessel function of the first kind of order $\nu$. Then, by applying the double exponential transform (e.g., in [28]) to (1.6), we obtain the following highly efficient numerical approach to compute the fractional Laplacian of an RBF kernel in [24]:

$$(-\Delta)^{\gamma/2}\phi(r) \approx \begin{cases} hr^{-\gamma+1-d} \sum\limits_{n=-N}^{N} j_n^{\frac{d}{2}+\gamma} (\mathcal{F}\phi)(\frac{j_n}{r}) J_{\frac{d}{2}-1}(j_n) \frac{w_n^j}{r}, & r \neq 0, \\ h \sum\limits_{n=-N}^{N} j_n^{\frac{d}{2}+\gamma} (\mathcal{F}\phi)(j_n) w_n^j, & r = 0, \end{cases} \tag{1.7}$$

where $j_n = \mathfrak{M}\varphi(nh + \frac{(d-3)h}{4})$, $w_n^j = \mathfrak{M}\varphi'(nh + \frac{(d-3)h}{4})$, $s_n = \mathfrak{M}\varphi(nh)$, $w_n^s = \mathfrak{M}\varphi'(nh)$, $h$ is the mesh size for the trapezoid rule, $h\mathfrak{M} = \pi$, and $\varphi(t) = t/(1 - \exp(-2t - \alpha(1 - e^{-t}) - \beta(e^t - 1)))$, with $\beta = 1/4$, $\alpha = \beta/\sqrt{1 + \mathfrak{M}\ln(1 + \mathfrak{M})/(4\pi)}$. The numerical approach described in (1.7) for computing the integral fractional Laplacian of RBF kernels achieves nearly machine precision, as demonstrated in [24]. Furthermore, the collocation schemes based on extended domains for the fractional Poisson problem in (1.1) and (1.2) have shown the ability to deliver high accuracy and improved conditioning.

### *1.4. Main contributions and novelty of the work*

The development of highly accurate numerical approaches for evaluating the integral fractional Laplacian of RBF kernels, along with the demonstrated success of the collocation methods in [24], motivates us to extend this methodology to broader classes of fractional PDEs. A natural next step is the space-fractional heat equation. Our approach developed in [24] adopts a pseudo-spectral framework that is structurally better suited and more streamlined for nonlocal problems than localized RBF methods (e.g., the aforementioned RBF-differential quadrature method [17]). Moreover, the extended-domain technique employed in [24] was shown to improve accuracy and conditioning for fractional elliptic problems, in contrast to pseudo-spectral methods that do not use domain extension, such as [14]. As a result, the proposed approach in the current study that *integrates highly efficient evaluation of the fractional Laplacian* with an *extended-domain pseudo-spectral formulation* is promising for solving space-fractional heat equations accurately and efficiently. For more complex models, such as the fractional Stokes equations, we are further inspired by the effectiveness of the Leray projection method for the classical (integer-order) Stokes problem as demonstrated in [29], which provides a streamlined framework that delivers highly accurate results. By integrating the Leray projection with the numerical approach for evaluating the integral fractional Laplacian of RBF kernels in [24], we aim to establish an efficient solver for fractional Stokes equations—of particular interest due to their relevance in theoretical turbulence. These considerations collectively motivate the present study.

However, the application of the Leray projection (e.g., as in [29]) to space-fractional Stokes problems is not straightforward and must be handled with care to accommodate complex domains and to avoid violating the underlying physics. In particular, the construction of the Leray projection may involve collocation points outside the domain, as the proposed collocation schemes in this study for nonlocal problems on complex domains involve exterior collocation points. Additionally, some physical conditions that hold in the integer-order setting, e.g., the impermeable boundary condition, are not applicable in the fractional case, which prevents the use of the perpendicular component of the Leray projection from recovering the pressure (as was done in the integer-order case in [29]).

Below, we summarize our *main contributions and novelty:*

- We develop a novel and efficient RBF collocation method based on the pseudo-spectral global framework for fractional heat equations on complex domains, using extended-domain techniques. The proposed approach is able to attain relatively high spatial accuracy and

reasonable spatial-temporal accuracy with first-order time discretizations (e.g., the backward-Euler scheme in (2.15)), and can improve the conditioning of the resulting linear systems.

- We formulate a practical guideline ("rule of thumb") for placing collocation points that yields numerically stable results for fractional heat problems, based on a first-order time-discretization scheme and validated through extensive numerical experiments. This guideline also provides insights for collocation strategies for a broad range of time-dependent fractional problems.
- We propose a novel numerical Leray projection method for fractional Stokes problems, in which both the discrete projection operator and the collocation scheme can be formulated on an extended domain to effectively handle the problems on complex domains. This unified approach synergistically integrates the Leray projection, extended-domain techniques, and efficient numerical approximation of the integral fractional Laplacian to streamline the decoupling of the fractional Stokes system and deliver rapid convergence with highly accurate solutions, even on complex domains. Observe that the numerical Leray projection method in [29, 30] cannot be directly applied here because of the nonlocal boundary condition. In particular, the impermeable boundary condition cannot be satisfied in general, while the methods in [29, 30] depend on the impermeable boundary condition.

### *1.5. Layout of the paper*

The layout of the article is as follows. In Section 2, we design an RBF collocation scheme for the fractional heat equation using extended domains. In Section 3, we propose an RBF collocation scheme for the fractional Stokes equation utilizing Leray projection. Sections 4 and 5 respectively report the numerical results for fractional heat and fractional Stokes equations. Finally, a brief conclusion and discussion are presented in Section 6.

## 2. Collocation methods for fractional heat conduction problems

In this section, we consider collocation methods for a linear fractional heat conduction problem. We introduce our methods and discuss the stability of the resulting linear system.

Consider the following fractional heat conduction problem:

$$\partial_t u(\mathbf{x}, t) + (-\Delta)^{\gamma/2} u(\mathbf{x}, t) = f, \quad (\mathbf{x}, t) \in \Omega \times (0, T], \tag{2.1}$$

$$u(\mathbf{x}, t) = g(\mathbf{x}, t), \quad (\mathbf{x}, t) \in \Omega^c \times [0, T], \tag{2.2}$$

$$u(\mathbf{x}, 0) = u_0(\mathbf{x}), \quad \mathbf{x} \in \Omega. \tag{2.3}$$

Following the idea in [24] and referring to (1.5), let $u_N(\mathbf{x}, t)$ be an RBF approximation of $u$, and then the RBF scheme corresponding to problems (2.1)–(2.3) can then be formulated with an extended domain $\widetilde{\Omega}$, as follows:

$$\partial_t u_N + (-\Delta)^{\gamma/2} u_N + \mathcal{B} u_N = f, \quad (\mathbf{x}, t) \in \Omega \times (0, T], \tag{2.4}$$

$$u_N(\mathbf{x}, t) = g(\mathbf{x}, t), \quad (\mathbf{x}, t) \in (\widetilde{\Omega} \setminus \Omega) \times [0, T], \tag{2.5}$$

$$u_N(\mathbf{x}, 0) = u_0(\mathbf{x}), \quad \mathbf{x} \in \Omega, \tag{2.6}$$

where

$$\mathcal{B}u(\mathbf{x}, t) = c_{d,\gamma} \int_{\widetilde{\Omega}^c} \frac{u(\mathbf{y}, t) - g(\mathbf{y}, t)}{|\mathbf{x} - \mathbf{y}|^{d+\gamma}} \, d\mathbf{y}, \quad \mathbf{x} \in \Omega.$$

Denote, for $\mathbf{x} \in \Omega$,

$$\mathcal{L}u := -(-\Delta)^{\gamma/2}u - c_{d,\gamma}\int_{\widetilde{\Omega}^c} \frac{u(\mathbf{y},t)}{|\mathbf{x}-\mathbf{y}|^{d+\gamma}}\,d\mathbf{y},\ \ \tilde{g} := \int_{\widetilde{\Omega}^c} \frac{g(\mathbf{y},t)}{|\mathbf{x}-\mathbf{y}|^{d+\gamma}}\,d\mathbf{y},$$

and then (2.4) can be re-written as

$$\partial_t u_N(\mathbf{x},t) - \mathcal{L}u_N(\mathbf{x},t) = f + c_{d,\gamma}\tilde{g}(\mathbf{x},t), \quad (\mathbf{x},t) \in \Omega \times (0,T]. \tag{2.7}$$

Throughout this paper, we define the collocation point sets: $X_I = \{\mathbf{x}_k\}_{k=1}^{N_I}$, $X_B = \{\mathbf{x}_k\}_{k=N_I+1}^{N_I+N_B}$, $X_E = \{\mathbf{x}_k\}_{k=N_I+N_B+1}^{N_I+N_B+N_E}$, respectively, in $\Omega$, on $\partial\Omega$, and in $\widetilde{\Omega} \setminus \overline{\Omega}$. We also denote $X_{BE} = X_B \cup X_E$, and the overall counts of the collocation points as $N = N_I + N_B + N_E$.

The collocation points $\{\mathbf{x}_k\}_{k=1}^N$ and the RBF centers $\{\mathbf{x}_j\}_{j=1}^N$ are not necessarily the same in general. However, in this work, we consider the case that they are coincident, which leads to desirable properties such as the symmetry and positive definiteness of the RBF interpolation matrix in (2.16). Then (2.5)–(2.7) yield the following *practical scheme* for the fractional heat conduction problem with collocation points deployed:

$$\partial_t u_N - \mathcal{L}u_N = f + c_{d,\gamma}\tilde{g}, \quad \text{on } (X_I,t) \subset \Omega \times (0,T], \tag{2.8}$$

$$u_N = g, \quad \text{on } (X_{BE},t) \subset \widetilde{\Omega} \setminus \Omega \times [0,T], \tag{2.9}$$

$$u_N(\mathbf{x},0) = u_0, \quad \text{on } X_I \subset \Omega. \tag{2.10}$$

Here the term $(-\Delta)^{\gamma/2}u_N$ can be computed with (1.7) as in [24]. The scheme described in (2.8)–(2.10) applies to the case where $\widetilde{\Omega} = \overline{\Omega}$, i.e., no extended domain or exterior points are included. In this scenario, the collocation scheme degenerates and becomes that in [14] if there is no time evolution. In this paper, we refer to the scheme with $\widetilde{\Omega} = \overline{\Omega}$ as Formulation I, and the scheme with $\overline{\Omega} \subsetneq \widetilde{\Omega}$ as Formulation II.

### *2.1. Backward Euler scheme in time*

Consider the uniform partition in time: $0 = t_0 < t_1 < \cdots < t_{N_t-1} = T$, with $N_t > 2$ and $N_t \in \mathbb{N}^+$. The backward Euler scheme for (2.7) can be written as

$$u^{n+1} - \tau\mathcal{L}u^{n+1} = u^n + \tau\left(f^{n+1} + c_{d,\gamma}\tilde{g}^{n+1}\right), \quad \mathbf{x} \in \Omega. \tag{2.11}$$

Here, we have denoted $u^k = u_N(\mathbf{x},t_k)$, $f^k = f(\mathbf{x},t_k)$, $\tilde{g}^k = \tilde{g}(\mathbf{x},t_k)$. Let $\phi(r)$ be an RBF kernel, and then

$$u_N(\mathbf{x},t) = \sum_{j=1}^N \tilde{u}_j(t)\phi(|\mathbf{x}-\mathbf{x}_j|) = \sum_{j=1}^N \tilde{u}_j(t)\phi_j(\mathbf{x}). \tag{2.12}$$

To facilitate the descriptions in this section, we also introduce the following **notations of discrete functions and vectors**: $\tilde{u}_j^k = \tilde{u}_j(t_k)$, $g^k = g(\mathbf{x},t_k)$, $\tilde{g}^k = \tilde{g}(\mathbf{x},t_k)$, $\mathbf{u}^k = (u_1^k,\cdots,u_N^k)^\top$, $\tilde{\mathbf{u}}^k = (\tilde{u}_1(t_k),\cdots,\tilde{u}_N(t_k))^\top$. With collocation points $\mathbf{x}_i$, we define $u_i^j = u_N(\mathbf{x}_i,t_j)$, $\mathbf{f}^k = (f(\mathbf{x}_1,t_k),...,f(\mathbf{x}_{N_I},t_k))^\top$, $\tilde{\mathbf{g}}^k = (\tilde{g}(\mathbf{x}_1,t_k),...,\tilde{g}(\mathbf{x}_{N_I},t_k))^\top$, $\mathbf{g}_{BE}^k = (g(\mathbf{x}_{N_I+1},t_k),...,g(\mathbf{x}_N,t_k))^\top$. Then (2.11) and (2.12) imply

$$\sum_{j=1}^N \tilde{u}_j^{n+1}\phi_j(\mathbf{x}_i) - \tau\sum_{j=1}^N \tilde{u}_j^{n+1}\mathcal{L}\phi_j(\mathbf{x}_i) = u^n(\mathbf{x}_i) + \tau\left(f^{n+1}(\mathbf{x}_i) + c_{d,\gamma}\tilde{g}^{n+1}(\mathbf{x}_i)\right),\ i = 1,2,...,N_I. \tag{2.13}$$

For $\mathbf{x}_i \in \widetilde{\Omega} \setminus \Omega$, $i = N_I + 1, ..., N$, we have

$$\sum_{j=1}^{N} \tilde{u}_j^{n+1} \phi_j(\mathbf{x}_i) = g^{n+1}(\mathbf{x}_i), \ i = N_I + 1, ..., N. \tag{2.14}$$

Now denote $H_j(\mathbf{x}) = \phi_j(\mathbf{x}) - \tau \mathcal{L}\phi_j(\mathbf{x})$, $\tilde{f}^{n+1} = f^{n+1} + c_{d,\gamma}\tilde{g}^{n+1}$. Then (2.13) and (2.14) yield the following matrix form:

$$M\tilde{\mathbf{u}}^{n+1} := \begin{bmatrix} H_1(\mathbf{x}_1) & \cdots & H_N(\mathbf{x}_1) \\ \vdots & \vdots & \vdots \\ H_1(\mathbf{x}_{N_I}) & \cdots & H_N(\mathbf{x}_{N_I}) \\ \phi_1(\mathbf{x}_{N_I+1}) & \cdots & \phi_N(\mathbf{x}_{N_I+1}) \\ \vdots & \vdots & \vdots \\ \phi_1(\mathbf{x}_N) & \cdots & \phi_N(\mathbf{x}_N) \end{bmatrix} \begin{bmatrix} \tilde{u}_1^{n+1} \\ \vdots \\ \tilde{u}_{N_I}^{n+1} \\ \tilde{u}_{N_I+1}^{n+1} \\ \vdots \\ \tilde{u}_N^{n+1} \end{bmatrix} = \begin{bmatrix} u^n(\mathbf{x}_1) + \tau \tilde{f}^{n+1}(\mathbf{x}_1) \\ \vdots \\ u^n(\mathbf{x}_{N_I}) + \tau \tilde{f}^{n+1}(\mathbf{x}_{N_I}) \\ g^{n+1}(\mathbf{x}_{N_I+1}) \\ \vdots \\ g^{n+1}(\mathbf{x}_N) \end{bmatrix}. \tag{2.15}$$

Since the time evolution occurs only within $\Omega$, where the governing equation (2.8) is defined, we derive the operator form in the following subsection. This aims to better identify the transmission factor between time layers that impacts stability and to achieve a consistent implementation format with the fractional Stokes problem to be discussed in Section 3.

### *2.2. The collocation methods in operational matrix form*

Consider the following RBF interpolation matrix:

$$\Phi = \begin{bmatrix} \phi_1(\mathbf{x}_1) & \cdots & \phi_N(\mathbf{x}_1) \\ \vdots & \vdots & \vdots \\ \phi_1(\mathbf{x}_N) & \cdots & \phi_N(\mathbf{x}_N) \end{bmatrix}. \tag{2.16}$$

We introduce a discrete operator $\mathcal{L}_h$ corresponding to $\mathcal{L}$, with $\mathcal{L}_h\Phi$ defined component-wise as follows:

$$(\mathcal{L}_h\Phi)_{i,j} := \mathcal{L}(\phi_i(\mathbf{x}))|_{\mathbf{x}=\mathbf{x}_j}, \ i, j = 1, 2, \ldots, N.$$

Also, for a function $v(\mathbf{x}, t)$, if we denote $\mathbf{v}_M = (v(\mathbf{x}_1, t), \ldots, v(\mathbf{x}_M, t))^\top$ as a vector that contains its evaluations at collocation points $\{\mathbf{x}_i\}_{i=1}^M$, then $\mathcal{L}_h\mathbf{v}_M$ is defined as

$$\mathcal{L}_h\mathbf{v}_M := (\mathcal{L}v(\mathbf{x}, t)\big|_{\mathbf{x}=\mathbf{x}_1}, \ldots, \mathcal{L}v(\mathbf{x}, t)\big|_{\mathbf{x}=\mathbf{x}_M})^\top.$$

We denote

$$L := (\mathcal{L}_h\Phi)\Phi^{-1}. \tag{2.17}$$

Here, we note that using a strictly positive definite kernel ensures that the interpolation matrix $\Phi$ in (2.16) is symmetric positive definite, and hence invertible. The Gaussian and Matern kernels considered in this study are strictly positive definite ( [31, p. 95], [32]), thus guaranteeing the invertibility of $\Phi$. Utilizing (2.12), we have

$$\mathbf{u}^{n+1} = \Phi\tilde{\boldsymbol{u}}^{n+1}, \tag{2.18}$$

and combining (2.17), we have

$$\mathcal{L}_h \mathbf{u}^{n+1} = \mathcal{L}_h \Phi \tilde{\mathbf{u}}^{n+1} = L\mathbf{u}^{n+1}. \tag{2.19}$$

Now we define the following sub-matrices of $L$:

$$L_I = L(1 : N_I, 1 : N_I),\ L_{BE} = L(1 : N_I, N_I + 1 : N).$$

Here, a notation such as $1{:}N_I$ follows MATLAB style, meaning it is used to extract specific rows or columns of a matrix. Then $L_I$ is the matrix that operates on interior nodes and $L_{BE}$ operates on boundary and exterior nodes. We extract the values of $\mathbf{u}^{n+1}$ corresponding to the interior evaluation points, denoted by $\mathbf{u}_I^{n+1}$, and the values corresponding to the boundary and exterior points, denoted by $\mathbf{u}_{BE}^{n+1}$, respectively. Then from (2.19), we have

$$\mathcal{L}_h \mathbf{u}_I^{n+1} = L_I \mathbf{u}_I^{n+1} + L_{BE} \mathbf{u}_{BE}^{n+1}. \tag{2.20}$$

Then according to (2.11), we have the **matrix form**

$$(I - \tau L_I)\mathbf{u}_I^{n+1} = \mathbf{u}_I^n + \tau \left( \mathbf{f}^{n+1} + c_{d,\gamma} \tilde{\mathbf{g}}^{n+1} + L_{BE} \mathbf{g}_{BE}^{n+1} \right). \tag{2.21}$$

Let $\lambda$ be the eigenvalues of $L_I$, and then the stability of the time evolution can be quantified by $(I - \tau\lambda)$. We define the transmission factor as follows.

**Definition 2.1.** Let $\lambda$ be the eigenvalues of $L_I$. Given a temporal step size $\tau$, the transmission factor $\eta$ for the backward Euler collocation scheme (2.21) for the fractional heat equation is: $\eta = \min |1 - \tau\lambda|$.

It can be readily verified that $\eta$ in the previous definition equals $\min |\lambda(M_I)|$, where $\lambda(M_I)$ are eigenvalues of $M_I$, $M_I = \widetilde{M}(1 : N_I, 1 : N_I)$, with $\widetilde{M} = M\Phi^{-1}$, and $M$ and $\Phi$ are defined in (2.15) and (2.16). A stable collocation scheme for fractional heat equations requires $\eta \geq 1$.

## 3. Collocation methods for fractional Stokes problems

In this section, we consider collocation methods for a fractional Stokes equation. We introduce our methods and discuss key differences between the projection methods for the classical Stokes equation (e.g., [29]) and the fractional Stokes equation. Consider the following incompressible fractional Stokes problem:

$$\partial_t \boldsymbol{u} + \nabla p = \nu \Delta \mathbf{u} - (-\Delta)^{\gamma/2} \mathbf{u} + \mathbf{f}, \quad (\mathbf{x}, t) \in \Omega \times (0, T], \tag{3.1}$$

$$\mathbf{u} = \mathbf{g}, \quad (\mathbf{x}, t) \in \Omega^c \times [0, T], \tag{3.2}$$

$$\mathbf{u}(\mathbf{x}, 0) = \mathbf{u}_0, \quad \mathbf{x} \in \Omega, \tag{3.3}$$

$$\nabla \cdot \mathbf{u} = 0, \quad (\mathbf{x}, t) \in \Omega \times (0, T]. \tag{3.4}$$

We note that (3.1) includes both the classical Laplacian and fractional Laplacian operators, which represent distinct dissipation mechanisms, with the former modeling molecular viscous dissipation and the latter accounting for nonlocal momentum transfer and anomalous dissipation. This mixed local-nonlocal model distinguishes itself from the classical Stokes equations (where only the classical Laplacian is present), and the mixed operator is commonly used for modeling turbulence and fractional fluid dynamics (see, e.g., [4, 5]).

Then, similar to the derivation of the fractional heat problem, an RBF collocation scheme corresponding to (3.1) and (3.2) can be formulated as follows:

$$\partial_t \mathbf{u}_N + \nabla p_N = \mathcal{L}\mathbf{u}_N + \mathbf{f} + c_{d,\gamma}\tilde{\mathbf{g}}, \quad (\mathbf{x}, t) \subset \Omega \times (0, T],$$
$$\mathbf{u}_N = \mathbf{g}, \quad (\mathbf{x}, t) \subset \widetilde{\Omega} \setminus \Omega \times [0, T],$$

where $\mathbf{u}_N$ and $p_N$ are the RBF approximations of $\mathbf{u}$ and $p$, respectively, and

$$\mathcal{L}\mathbf{u} := \nu\Delta\mathbf{u} - (-\Delta)^{\gamma/2}\mathbf{u} - c_{d,\gamma}\int_{\widetilde{\Omega}^c} \frac{\mathbf{u}(\mathbf{y}, t)}{|\mathbf{x} - \mathbf{y}|^{d+\gamma}}\, d\mathbf{y}, \tag{3.5}$$

$$\tilde{\mathbf{g}} := c_{d,\gamma}\int_{\widetilde{\Omega}^c} \frac{\mathbf{g}(\mathbf{y}, t)}{|\mathbf{x} - \mathbf{y}|^{d+\gamma}}\, d\mathbf{y}. \tag{3.6}$$

With collocation points deployed, it becomes the following practical RBF collocation scheme:

$$\partial_t \mathbf{u}_N + \nabla p_N = \mathcal{L}\mathbf{u}_N + \mathbf{f} + c_{d,\gamma}\tilde{\mathbf{g}}, \quad \text{on } (X_I, t) \subset \Omega \times (0, T], \tag{3.7}$$
$$\mathbf{u}_N = \mathbf{g}, \quad \text{on } (X_{BE}, t) \subset \widetilde{\Omega} \setminus \Omega \times [0, T]. \tag{3.8}$$

We still refer to the scheme with $\widetilde{\Omega} = \overline{\Omega}$ as Formulation I, and the scheme with $\overline{\Omega} \subsetneq \widetilde{\Omega}$ as Formulation II.

### *3.1. Divergence-free kernel (Leray projection) method*

According to [33, 34], a given vector field $\mathbf{w}$ can be decomposed as

$$\mathbf{w} = \nabla q + \mathbf{v}, \tag{3.9}$$

with $\nabla \cdot \mathbf{v} = 0$. This decomposition, known as Helmholtz–Hodge [34] decomposition of $\mathbf{w}$, exists and is unique up to an additive constant for $q$. Then the Leray projection $\Pi$ can be defined such that $\Pi(\mathbf{w}) = \mathbf{v}$, $\Pi(\mathbf{v}) = \mathbf{v}$, and $\Pi(\nabla q) = 0$. Applying the Leray projection $\Pi$ to the governing equation of the fractional Stokes problem (3.1), it follows that

$$\partial_t \mathbf{u} = \Pi(\nu\Delta\mathbf{u} - (-\Delta)^{\gamma/2}\mathbf{u} + \mathbf{f}), \quad (\mathbf{x}, t) \in \Omega \times (0, T],$$

where we have used the fact that $\Pi(\partial_t \mathbf{u}) = \partial_t \mathbf{u}$, $\Pi(\nabla p) = 0$. We employ a matrix $\mathbb{P}_{\text{div}}$—a discrete Leray projection—to approximate the continuous operator $\Pi$ and apply it to (3.7). Combining this with (3.8), we formulate a *practical RBF collocation scheme* for $\mathbf{u}_N$ based on the *discrete Leray projection* as follows:

$$\partial_t \mathbf{u}_N = \mathbb{P}_{\text{div}}(\mathcal{L}\mathbf{u}_N + c_{d,\gamma}\tilde{\mathbf{g}} + \mathbf{f}), \quad \text{on } (X_I, t) \in \Omega \times (0, T], \tag{3.10}$$
$$\mathbf{u}_N = \mathbf{g}, \quad \text{on } (X_{BE}, t) \in \widetilde{\Omega} \setminus \Omega \times [0, T]. \tag{3.11}$$

#### 3.1.1. Approximate Leray projector $\Pi$

Inspired by the approach in [29, 30], we now describe the construction of the discrete Leray projection $\mathbb{P}_{\text{div}}$. Note that the divergence-free and curl-free matrix-valued kernels are defined as [29,35]

$$\Phi_{\text{div}} = \left(-\Delta I + \nabla\nabla^T\right)\phi, \quad \Phi_{\text{curl}} = -\nabla\nabla^T\phi,$$

respectively, where $\phi$ is a standard scalar-valued RBF and $I \in \mathbb{R}^{d\times d}$ is an identity matrix. $\Phi_{\text{div}}$ consists of divergence-free columns, while $\Phi_{\text{curl}}$ is composed of columns that are curl-free [30]. The kernel $\Phi_a$, termed as the full kernel [29], is defined as

$$\Phi_a = \Phi_{\text{div}} + \Phi_{\text{curl}} = -\Delta\phi I.$$

In this work, we focus on the case $d = 2$ (i.e., the two-dimensional case). Denoting $r = \|\mathbf{x} - \mathbf{x}_j\|_2$, $\chi = \phi'(r)/r$, and $\psi = \chi'(r)/r$, $\Phi_{\text{div}}$ and $\Phi_{\text{curl}}$ take the following forms [29]:

$$\Phi_{\text{div}}(\mathbf{x}, \mathbf{x}_j) = \begin{bmatrix} a & b \\ b & c \end{bmatrix}, \ \Phi_{\text{curl}}(\mathbf{x}, \mathbf{x}_j) = \begin{bmatrix} c & -b \\ -b & a \end{bmatrix}. \tag{3.12}$$

Here, $a = -\chi(r) - \psi(r)(y - y_j)^2$, $b = \psi(r)(x - x_j)(y - y_j)$, $c = -\chi(r) - \psi(r)(x - x_j)^2$. For a vector field $\mathbf{f}$, inspired by [29], an interpolant that coincides with $\mathbf{f}$ at the interior nodes $X_I$ and also satisfies the divergence-free nonlocal boundary condition $\mathbf{g}$ on the boundary and exterior nodes $X_{BE}$ can be constructed as follows:

$$s_{\mathbf{f}} = \sum_{k=1}^{N_I} \mathbf{c}_k \Phi_a(\cdot, \mathbf{x}_k) + \sum_{j=1}^{N_B+N_E} \mathbf{d}_j \Phi_{\text{div}}(\cdot, \mathbf{x}_{j+N_I}),$$

where $\mathbf{c}_k = (c_{k,1}, c_{k,2})^\top, \mathbf{d}_k = (d_{k,1}, d_{k,2})^\top$. For $k, l = 1, \ldots, N_I$ and $i, j = 1, \ldots, N_B + N_E$, we define the following $2 \times 2$ real block matrices:

$$A_{k,l} = \Phi_a(\mathbf{x}_k, \mathbf{x}_l), \ B_{k,j} = \Phi_{\text{div}}(\mathbf{x}_k, \mathbf{x}_{j+N_I}), \ C_{i,j} = \Phi_{\text{div}}(\mathbf{x}_{i+N_I}, \mathbf{x}_{j+N_I}). \tag{3.13}$$

Then we have $A \in \mathbb{R}^{2N_I\times 2N_I}$, $B \in \mathbb{R}^{2N_I\times 2(N_B+N_E)}$, $C \in \mathbb{R}^{2(N_B+N_E)\times 2(N_B+N_E)}$. Implementing the interpolation conditions with

$$\begin{aligned} s_{\mathbf{f}}(\mathbf{x}_k) &= \mathbf{f}(\mathbf{x}_k), \ k = 1, 2, ..., N_I, \\ \mathbb{P}_{\text{div}} s_{\mathbf{f}}(\mathbf{x}_{j+N_I}) &= \mathbf{g}(\mathbf{x}_{j+N_I}), \ j = 1, 2, ..., N_B + N_E, \end{aligned}$$

yields the following matrix form:

$$\begin{bmatrix} A & B \\ B^\top & C \end{bmatrix} \begin{bmatrix} \mathbf{c} \\ \mathbf{d} \end{bmatrix} = \begin{bmatrix} \mathbf{f}_I \\ \mathbf{g}_{BE} \end{bmatrix}. \tag{3.14}$$

In practice, to facilitate implementation, we follow [29] and reorganize the matrices $A$, $B$, and $C$ into $2 \times 2$ block structures. Each block corresponds to a specific component-wise evaluation of the kernel functions—for instance, the upper-left block involves evaluations of the upper-left components of the kernels (as defined in (3.12)), the upper-right block collects the upper-right component evaluations, and likewise for the remaining blocks. Letting $\widetilde{A}$, $\widetilde{B}$, and $\widetilde{C}$ denote the reordered versions of the original matrices, (3.14) can now be rewritten as

$$\begin{bmatrix} \widetilde{A} & \widetilde{B} \\ \widetilde{B}^\top & \widetilde{C} \end{bmatrix} \begin{bmatrix} \tilde{\mathbf{c}} \\ \tilde{\mathbf{d}} \end{bmatrix} = \begin{bmatrix} \mathbf{f}_I^x \\ \mathbf{f}_I^y \\ \mathbf{g}_{BE}^x \\ \mathbf{g}_{BE}^y \end{bmatrix},$$

where the right-hand-side vectors have been rearranged accordingly so that $\mathbf{f}_I^x$ and $\mathbf{f}_I^y$ are $x$ and $y$ components of $\mathbf{f}$ evaluated at $X_I$, and $\mathbf{g}_{BE}^x$ and $\mathbf{g}_{BE}^y$ are $x$ and $y$ components of $\mathbf{g}$ evaluated at $X_{BE}$.

To simplify the notation, although we use $A$ indeed, we will denote it as $A$, and similarly for other matrices involved, throughout the remainder of the paper. Then $\Pi(\mathbf{f})$ can be approximated by the following $\mathbb{P}_{\text{div}}\boldsymbol{s}_{\mathbf{f}}$:

$$\Pi(\mathbf{f}) \approx \mathbb{P}_{\text{div}}\boldsymbol{s}_{\mathbf{f}} = \sum_{k=1}^{N_I} \mathbf{c}_k \Phi_{\text{div}}(\cdot, \mathbf{x}_k) + \sum_{j=1}^{N_B+N_E} \mathbf{d}_j \Phi_{\text{div}}(\cdot, \mathbf{x}_{j+N_I}). \tag{3.15}$$

Finally, (3.14) and (3.15) yield the discrete Leray projector $\mathbb{P}_{\text{div}}$:

$$\mathbb{P}_{\text{div}} = [P_I \; P_{BE}] = [A_{\text{div}} \; B] \begin{bmatrix} A & B \\ B^\top & C \end{bmatrix}^{-1} := [A_{\text{div}} \; B] G^{-1}, \tag{3.16}$$

where $A_{\text{div}}$ is the divergence-free-kernel counterpart of $A$ (i.e., replace $\Phi_a$ by $\Phi_{\text{div}}$), $P_I \in \mathbb{R}^{2N_I \times 2N_I}$, $P_{BE} \in \mathbb{R}^{2N_I \times 2(N_B+N_E)}$.

### 3.1.2. Recover the pressure

For a vector field $\mathbf{w}$, recall the Helmholtz-Hodge decomposition in (3.9), we specify $\mathbf{v} = \partial_t \mathbf{u}, \nabla q = \nabla p$, with $\partial_t \mathbf{u}, \nabla p$ from the fractional Stokes governing equation (3.1). Then combining (3.1), $\mathbf{w}$ takes the following form:

$$\mathbf{w} = \partial_t \boldsymbol{u} + \nabla p = \nu \Delta \mathbf{u} - (-\Delta)^{\frac{\gamma}{2}} \mathbf{u} + \mathbf{f}. \tag{3.17}$$

It is important to note that, according to [36] and Proposition 2.1 in [30], the relation $\nabla q \perp \mathbf{v}$ ($\nabla p \perp \partial_t \mathbf{u}$) holds under the condition that $\mathbf{v} \cdot \mathbf{n} = 0$ on $\partial\Omega$. This condition is satisfied, for instance, when the *impermeable boundary condition* $\mathbf{u} \cdot \mathbf{n} = 0$ is imposed, as was done in [29]. However, enforcing this impermeable boundary condition is generally incompatible with the physics of the *fractional Stokes equations*, where a non-zero velocity field may exist outside the domain (i.e., in $\overline{\Omega}^c$). Therefore, in the fractional setting, imposing the impermeable condition $\mathbf{u} \cdot \mathbf{n} = 0$ to guarantee $\nabla q \perp \mathbf{v}$ is physically incompatible.

As a result, in the fractional Stokes problem considered, $\nabla q \not\perp \mathbf{v}$ ($\nabla p \not\perp \partial_t \mathbf{u}$). In this case, although the Leray projector $\Pi$ can be used to decouple the velocity and pressure in (3.17)—specifically, yielding $\Pi(\mathbf{w}) = \Pi(\partial_t \mathbf{u}) = \Pi\left(\nu \Delta \mathbf{u} - (-\Delta)^{\gamma/2} \mathbf{u} + \mathbf{f}\right)$, we are *unable* to recover the pressure $p$ via the curl-free projector $P_{\text{curl}}$. This is because it is readily verified that when $\nabla p \not\perp \partial_t \mathbf{u}$, it follows that $P_{\text{curl}} \neq \Pi^\perp$. Therefore, applying $P_{\text{curl}}$ to $\mathbf{w}$ does not extract the pressure $p$ in the same manner as in Eqs (4) and (27) of [29]. (In [29], $P_{\text{curl}} = \Pi^\perp$, thus $P_{\text{curl}}\mathbf{w} = \Pi^\perp \mathbf{w} = \Pi^\perp(\nabla p) = P_{\text{curl}}(\nabla p)$, and then $p$ can be exacted using the curf-free kernel. However, this is *not the case* in the current study.)

A common practice to recover the pressure term is to solve an auxiliary Poisson problem about $p$ [35, 37]. To be specific, applying the divergence operator to (3.17), and combining the Neumann boundary condition, we can formulate an auxiliary problem about $p$ as follows:

$$\Delta p = \nabla \cdot (\nu \Delta \mathbf{u} - (-\Delta)^{\frac{\gamma}{2}} \mathbf{u} + \mathbf{f}), \quad (\mathbf{x}, t) \in \Omega \times (0, T], \tag{3.18}$$

$$\nabla p \cdot \mathbf{n} = (\mathbf{f} + \nu \Delta \mathbf{u} - (-\Delta)^{\frac{\gamma}{2}} \mathbf{u} - \partial_t \mathbf{u}) \cdot \mathbf{n}, \quad (\mathbf{x}, t) \in \partial\Omega \times (0, T]. \tag{3.19}$$

When using an RBF function $p_N$ to approximate $p$, considering (3.7), the corresponding auxiliary problem regarding $p_N$ with collocation points can be formulated as follows:

$$\Delta p_N = \nabla \cdot (\mathcal{L}\mathbf{u}_N + \mathbf{f} + c_{d,\gamma}\tilde{\mathbf{g}}), \quad \text{on } (\{\mathbf{x}_k\}_{k=1}^{N_I}, t) \in \Omega \times (0, T], \tag{3.20}$$

$$\nabla p_N \cdot \mathbf{n} = (\mathbf{f} + \mathcal{L}\mathbf{u}_N + c_{d,\gamma}\tilde{\mathbf{g}} - \partial_t \mathbf{u}_N) \cdot \mathbf{n}, \quad \text{on } (\{\mathbf{x}_k\}_{k=N_I+1}^{N}, t) \in \partial\Omega \times (0, T]. \tag{3.21}$$

We note that when solving the auxiliary problems (3.20) and (3.21), approximating $\partial_t \mathbf{u}_N$ is unavoidable, as the boundary term $\partial_t \mathbf{u}_N \cdot \mathbf{n}$ cannot be eliminated due to the lack of an applicable impermeable condition. Likewise, the term $\mathcal{L}\mathbf{u}_N \cdot \mathbf{n}$ cannot be canceled on $\partial\Omega$, necessitating an extension of $\mathcal{L}\mathbf{u}_N$ to the boundary. A similar extension is also required for $\tilde{\mathbf{g}}$. However, extending $\tilde{\mathbf{g}}$ to $\mathbf{x} \in \partial\Omega$ can amplify its weak singularity, as indicated by its definition in (3.6). These approximations and boundary extensions may affect the accuracy of the auxiliary problems (3.20) and (3.21), and likely require specialized treatment to address properly.

As a first and crucial step toward accurate pressure reconstruction, in this work, we focus on evaluating the accuracy of pressure gradient reconstruction by directly computing $\nabla p_N$ from the RBF scheme (3.7), i.e.,

$$\nabla p_N = \mathbf{f} + \mathcal{L}\mathbf{u}_N + c_{d,\gamma}\tilde{\mathbf{g}} - \partial_t \mathbf{u}_N, \quad \text{on } (\{\mathbf{x}_k\}_{k=1}^{N_I}, t) \in \Omega \times (0, T]. \tag{3.22}$$

This $\nabla p_N$ will be used to approximate $\nabla p$ and be recorded in the numerical results in Section 5. A comprehensive investigation of the auxiliary problem about $p$ and its accurate numerical treatment is left as an important direction for future research.

### *3.2. BDF2 scheme*

We consider $\mathcal{L}$ in (3.5) and the RBF interpolation matrix $\Phi$ in (2.16), as well as the discrete operator $\mathcal{L}_h$ corresponding to $\mathcal{L}$ (cf. Section 2.2 for the relation between $\mathcal{L}$ and $\mathcal{L}_h$). Then we define $L := \Phi^{-1}\mathcal{L}_h\Phi$, and the following sub-matrices of $L$:

$$L_I = L(1 : N_I, 1 : N_I), \; L_{BE} = L(1 : N_I, N_I + 1 : N_I + N_B + N_E).$$

We also introduce the following notation related to (3.7). The $x$ and $y$ components, evaluated at the indicated points for a function, are denoted as follows: $\mathbf{u}_I, \mathbf{v}_I$ for $\mathbf{u}$ evaluated at $X_I$; $(\mathbf{p}_x)_I, (\mathbf{p}_y)_I$ for $\nabla p$ at $X_I$; $\mathbf{f}_I^x, \mathbf{f}_I^y$ for $\mathbf{f}$ at $X_I$; $\tilde{\mathbf{g}}^x, \tilde{\mathbf{g}}^y$ for $\tilde{\mathbf{g}}$ at $X_I$; and $\mathbf{g}_{BE}^x, \mathbf{g}_{BE}^y$ for $\mathbf{g}$ at $X_{BE}$. For these functions, when a superscript $k$ appears, it indicates evaluation at $t = t_k$, with $\{t_k\}_{k=0}^{M}$ a uniform time partition of $[0, T]$.

Therefore (3.7) becomes

$$\frac{d}{dt}\begin{bmatrix}\mathbf{u}_I\\ \mathbf{v}_I\end{bmatrix} + \begin{bmatrix}(\mathbf{p}_x)_I\\ (\mathbf{p}_y)_I\end{bmatrix} = \begin{bmatrix}L_I & \\ & L_I\end{bmatrix}\begin{bmatrix}\mathbf{u}_I\\ \mathbf{v}_I\end{bmatrix} + \begin{bmatrix}L_{BE}\mathbf{g}_{BE}^x\\ L_{BE}\mathbf{g}_{BE}^y\end{bmatrix} + \begin{bmatrix}\mathbf{f}_I^x\\ \mathbf{f}_I^y\end{bmatrix} + c_{d,\gamma}\begin{bmatrix}\tilde{\mathbf{g}}^x\\ \tilde{\mathbf{g}}^y\end{bmatrix} + \frac{d}{dt}\begin{bmatrix}\mathbf{g}_{BE}^x\\ \mathbf{g}_{BE}^y\end{bmatrix}. \tag{3.23}$$

Applying the discrete Leray projector in (3.16) to the above equation, it follows that

$$\frac{d}{dt}\begin{bmatrix}\mathbf{u}_I\\ \mathbf{v}_I\end{bmatrix} = P_I\left(\begin{bmatrix}L_I & \\ & L_I\end{bmatrix}\begin{bmatrix}\mathbf{u}_I\\ \mathbf{v}_I\end{bmatrix} + \begin{bmatrix}L_{BE}\mathbf{g}_{BE}^x\\ L_{BE}\mathbf{g}_{BE}^y\end{bmatrix} + \begin{bmatrix}\mathbf{f}_I^x\\ \mathbf{f}_I^y\end{bmatrix} + c_{d,\gamma}\begin{bmatrix}\tilde{\mathbf{g}}^x\\ \tilde{\mathbf{g}}^y\end{bmatrix}\right) + P_{BE}\frac{d}{dt}\begin{bmatrix}\mathbf{g}_{BE}^x\\ \mathbf{g}_{BE}^y\end{bmatrix}.$$

Then we discretize the time with the following *BDF2 scheme*:

$$M_1\begin{bmatrix}\mathbf{u}_I^{n+2}\\ \mathbf{v}_I{}^{n+2}\end{bmatrix} := \left(\begin{bmatrix}I & \\ & I\end{bmatrix} - \frac{2}{3}\tau P_I\begin{bmatrix}L_I & \\ & L_I\end{bmatrix}\right)\begin{bmatrix}\mathbf{u}_I^{n+2}\\ \mathbf{v}_I{}^{n+2}\end{bmatrix}$$

$$= \frac{4}{3}\begin{bmatrix}\mathbf{u}_I^{n+1}\\ \mathbf{v}_I{}^{n+1}\end{bmatrix} - \frac{1}{3}\begin{bmatrix}\mathbf{u}_I^{n}\\ \mathbf{v}_I{}^{n}\end{bmatrix} + \frac{2}{3}\tau P_I\left(\begin{bmatrix}L_{BE}(\mathbf{g}_{BE}^x)^{n+2}\\ L_{BE}(\mathbf{g}_{BE}^y)^{n+2}\end{bmatrix} + \begin{bmatrix}(\mathbf{f}_I^x)^{n+2}\\ (\mathbf{f}_I^y)^{n+2}\end{bmatrix} + c_{d,\gamma}\begin{bmatrix}(\tilde{\mathbf{g}}^x)^{n+2}\\ (\tilde{\mathbf{g}}^y)^{n+2}\end{bmatrix}\right)$$
$$+ P_{BE}\begin{bmatrix}\frac{3}{2}(\mathbf{g}_{BE}^x)^{n+2} - 2(\mathbf{g}_{BE}^x)^{n+1} + (\mathbf{g}_{BE}^x)^{n}\\ \frac{3}{2}(\mathbf{g}_{BE}^y)^{n+2} - 2(\mathbf{g}_{BE}^y)^{n+1} + (\mathbf{g}_{BE}^y)^{n}\end{bmatrix}. \tag{3.24}$$

Resorting to Chapters 6 and 7 of [38], the stability of the BDF2 scheme can be verified with the following theorem:

**Theorem 3.1.** Let $\lambda$ be the eigenvalues of $P_I\begin{bmatrix}L_I & \\ & L_I\end{bmatrix}$. The BDF2 collocation scheme (3.24) for the fractional Stokes equation is absolutely stable if $|\xi_i| \le 1$, $i = 1, 2$, where $\xi_i$ are roots of the equation $(\frac{3}{2} - z)\xi^2 - 2\xi + \frac{1}{2}$, with $z = \tau\lambda$.

The gradient of pressure can be recovered from (3.23) combining the BDF2 scheme with $(\mathbf{u}_I^{n+2}, \mathbf{v}_I^{n+2})^\top$ already known from (3.24). The details are illustrated as follows:

$$\begin{bmatrix}\mathbf{p}_x^{n+2}\\ \mathbf{p}_y^{n+2}\end{bmatrix} = \begin{bmatrix}\frac{3}{2}(\mathbf{g}_{BE}^x)^{n+2} - 2(\mathbf{g}_{BE}^x)^{n+1} + (\mathbf{g}_{BE}^x)^{n}\\ \frac{3}{2}(\mathbf{g}_{BE}^y)^{n+2} - 2(\mathbf{g}_{BE}^y)^{n+1} + (\mathbf{g}_{BE}^y)^{n}\end{bmatrix} - \begin{bmatrix}\frac{3}{2}\mathbf{u}_I^{n+2} - 2\mathbf{u}_I^{n+1} + \mathbf{u}_I^{n}\\ \frac{3}{2}\mathbf{v}_I^{n+2} - 2\mathbf{v}_I^{n+1} + \mathbf{v}_I^{n}\end{bmatrix} \tag{3.25}$$
$$+ \tau\left(\begin{bmatrix}L_I & \\ & L_I\end{bmatrix}\begin{bmatrix}\mathbf{u}_I^{n+2}\\ \mathbf{v}_I^{n+2}\end{bmatrix} + \begin{bmatrix}L_{BE}(\mathbf{g}_{BE}^x)^{n+2}\\ L_{BE}(\mathbf{g}_{BE}^y)^{n+2}\end{bmatrix} + \begin{bmatrix}(\mathbf{f}_I^x)^{n+2}\\ (\mathbf{f}_I^y)^{n+2}\end{bmatrix} + c_d^\gamma\begin{bmatrix}(\tilde{\mathbf{g}}^x)^{n+2}\\ (\tilde{\mathbf{g}}^y)^{n+2}\end{bmatrix}\right).$$

## 4. Numerical examples for fractional heat equations

In this section, we present two numerical examples for solving fractional heat problems in (2.8)–(2.10). We focus on the two-dimensional case (i.e, $d = 2$ in (2.8)). To be specific, we discuss the impact of employing Matern and Gaussian kernels for problems on different complex domains with different smoothness of solutions. Additionally, we explore the benefits of utilizing extended domains and provide a rule of thumb for placing collocation points that help maintain stability in time-dependent problems. The numerical solver utilizes the matrix form in (2.15), where cond($M$) in the tables represents the condition number of matrix $M$.

We measure solution accuracy using the root-mean-square (RMS) error. Specifically, for a scalar or vector-valued function $\mathbf{f}$ with an RBF approximation $\mathbf{f}_N$, and recalling that the interior collocation points $X_I = \{\mathbf{x}_j\}_{j=1}^{N_I}$, the RMS error is defined as

$$\|e_{\mathbf{f}}\|_{\text{rms}} = \left(\frac{1}{N_I}\sum_{j=1}^{N_I}\left\|\mathbf{f}(\mathbf{x}_j, T) - \mathbf{f}_N(\mathbf{x}_j, T)\right\|_2^2\right)^{1/2}.$$

Unless otherwise stated, in Section 4, $\|e\|_{\text{rms}}$ denotes the RMS error of the RBF approximation to $u$. To further examine the error, we also introduce $\|e_{\mathbf{f}}\|_I$, defined as the $L^2$ error over the domain $\Omega$, which is computed using Gauss–Legendre quadrature. Similarly, without stating otherwise, $\|e\|_I$ denotes the $L^2$ error of the RBF approximation to $u$.

For $\mathbf{x} \in \mathbb{R}^d$ ($d \ge 1$), the Matern RBF kernel takes the form: $\phi(\mathbf{x}) = \frac{(a|\mathbf{x}|)^\nu}{\Gamma(\nu)2^{\nu-1}}K_\nu(a|\mathbf{x}|)$, with $K_\nu$ the modified Bessel function of the second kind. The Gaussian RBF kernel takes the form: $\phi(\mathbf{x}) = \exp(-\epsilon|\mathbf{x}|^2)$ with a constant $\epsilon > 0$. In this paper, we take $a = 1, \nu = 5.5$, and $\epsilon = 0.1$. To

evaluate our method, we apply it to examples with *the following exact solutions* on two-dimensional domains. The analytical form of the fractional Laplacian of those solutions can be derived with the information in Appendix A of [24], and the source term $f$ can then be generated accordingly.

a) Algebraically decaying: $u = (1 + x^2 + y^2)^{-3/2} \sin(\pi t)$;
b) Compactly supported on a unit disk $\Omega$: $u = \left(1 - \min(x^2 + y^2, 1)\right)^{3+\gamma/2} \sin(\pi t)$;
c) Exponentially decaying: $u = \exp(-(x^2 + y^2)) \sin(\pi t)$.

In all numerical examples in this section, we let the time domain be $[0, 1]$. For time-dependent problems, the collocation points should be handled with more care compared to the steady-state problems, as it might violate the stability condition (i.e., the stability condition $\eta \geq 1$ in Definition 2.1) associated with the first-order time discretization scheme. We investigate the relation between the minimal distances and transmission factors by scattering different combinations of collocation points. Recall that $X_I, X_B, X_E$ represent the set of interior, boundary, and exterior collocation points, respectively. We denote (i) min All, (ii) min IB, (iii) min E, (iv) min BE, (v) min Ic, (vi) min Ec, respectively, to represent the minimal distances between points in the set of (1) $X_I \cup X_B \cup X_E$, (2) $X_I \cup X_B$, (3) $X_E$, (4) $X_B \cup X_E$, (5) $\text{dist}(X_I, \partial\Omega)$, and (6) $\text{dist}(X_E, \partial\Omega)$.

**Example 4.1** (Fractional heat equation, 3-petal domain)**.** We consider a 3-petal domain regulated by $\Omega = \{(r, \theta) \,|\, r < 0.7 + 0.2 \sin(3\theta), 0 \leq \theta < 2\pi\}$. The extended domain $\widetilde{\Omega}$ is a unit open disk centered at $(0, 0)$.

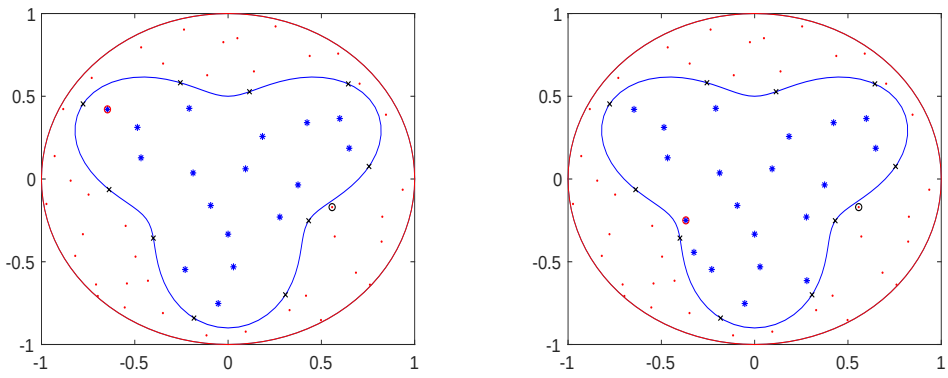


**Figure 1.** Sketch of 3-petal domain and scattering. Left: $(N_I, N_B, N_E) = (17, 10, 40)$; Right: $(N_I, N_B, N_E) = (20, 10, 40)$.

As indicated in Table 1, which corresponds to Figure 1, for the two combinations of the collocation points that have similar distributions, the major difference lies in min IB and min Ic. The combination (20,10,40) with smaller min IB and min Ic leads to $\eta < 1$, which incurs the non-stability in the time evolution. In Figure 1, the interior and exterior collocation points closest to $\partial\Omega$ are circled in red and black, respectively. We have also tested the other combinations and observed similar behavior. Therefore, a good practice of scattering is to avoid collocating the interior points too close to the boundary.

**Table 1.** Points distance comparison and resulting $\eta$ using the Matern kernel with $\gamma = 1.8, \tau = 1/64$ for Example 4.1.

| $(N_I, N_B, N_E)$ | min All | min IB | min E | min BE | min Ic | min Ec | $\eta$ |
|---|---|---|---|---|---|---|---|
| (17,10,40) | 0.06 | 0.13 | 0.07 | 0.06 | 0.12 | 0.03 | 1.15 |
| (20,10,40) | 0.06 | 0.09 | 0.07 | 0.06 | 0.06 | 0.03 | 0.93 |

As shown in Tables 2 and 3, for algebraically decaying solutions (which are smooth), both the Matern kernel and the Gaussian kernel deliver good and comparable accuracy, with the Gaussian kernel providing slightly better accuracy. However, we observe that the condition number when using the Gaussian kernel is significantly larger. This suggests that for smooth solutions, the Matern kernel serves as a more robust tool, as the Matern kernel with the parameter $\nu = 5.5$ exhibits considerable smoothness and provides better conditioning compared to the Gaussian kernel. We also record the corresponding $L^2$ errors in Table 4, and observe that they exhibit similar behavior to the RMS errors in Tables 2 and 3. Since the backward Euler scheme is employed, the error is dominated by the time step size. To facilitate the observation of spatial convergence, we select a smaller time step of $\tau = 1/1024$. The results, illustrated with the Matern kernel, and presented in Table 5, and measured in both RMS and $L^2$ norms, demonstrate spatial convergence with the increase in the number of collocation points. Similar phenomena are observed when the exact solution decays exponentially.

**Table 2.** RMS errors for Example 4.1 with the algebraically decaying solution using the Matern kernel when $t = 1$ with $\tau = 1/64$.

| $(N_I, N_B, N_E)$ | $\gamma = 1.2$ | | | $\gamma = 1.5$ | | | $\gamma = 1.8$ | | |
|---|---|---|---|---|---|---|---|---|---|
| | $\|\|e\|\|_{rms}$ | cond$(M)$ | $\eta$ | $\|\|e\|\|_{rms}$ | cond$(M)$ | $\eta$ | $\|\|e\|\|_{rms}$ | cond$(M)$ | $\eta$ |
| (17,10,40) | 6.7591e-03 | 7.75e+06 | 1.06 | 3.7737e-03 | 7.75e+06 | 1.10 | 1.8987e-03 | 7.76e+06 | 1.15 |
| (33,10,82) | 6.1534e-03 | 9.01e+08 | 1.07 | 3.1596e-03 | 9.00e+08 | 1.11 | 1.4951e-03 | 8.98e+08 | 1.16 |
| (46,20,113) | 5.1858e-03 | 1.61e+10 | 1.07 | 2.4638e-03 | 1.61e+10 | 1.12 | 1.0665e-03 | 1.61e+10 | 1.19 |

**Table 3.** RMS errors for Example 4.1 with the algebraically decaying solution using the Gaussian kernel when $t = 1$ with $\tau = 1/64$.

| $(N_I, N_B, N_E)$ | $\gamma = 1.2$ | | | $\gamma = 1.5$ | | | $\gamma = 1.8$ | | |
|---|---|---|---|---|---|---|---|---|---|
| | $\|\|e\|\|_{rms}$ | cond$(M)$ | $\eta$ | $\|\|e\|\|_{rms}$ | cond$(M)$ | $\eta$ | $\|\|e\|\|_{rms}$ | cond$(M)$ | $\eta$ |
| (17,10,40) | 6.5367e-03 | 4.89e+07 | 1.07 | 3.5283e-03 | 4.79e+07 | 1.10 | 1.7022e-03 | 4.69e+07 | 1.15 |
| (33,10,82) | 7.5325e-03 | 8.62e+12 | 1.04 | 4.4270e-03 | 9.35e+12 | 1.09 | 1.6712e-03 | 1.09e+13 | 1.19 |
| (46,20,113) | 4.1401e-03 | 2.21e+16 | 1.09 | 1.4464e-03 | 1.88e+16 | 1.16 | 5.3133e-04 | 3.23e+16 | 1.26 |

**Table 4.** $L^2$ errors for Example 4.1 with the algebraically decaying solution using Matern and Gaussian kernels when $t = 1$ with $\tau = 1/64$. Here, M. and G. are, respectively, abbreviations for Matern and Gaussian.

| $(N_I, N_B, N_E)$ | $\gamma = 1.2$ | | $\gamma = 1.5$ | | $\gamma = 1.8$ | |
|---|---|---|---|---|---|---|
| | $\|e\|_I$ (Matern) | $\|e\|_I$ (Gaussian) | $\|e\|_I$ (M.) | $\|e\|_I$ (G.) | $\|e\|_I$ (M.) | $\|e\|_I$ (G.) |
| (17,10,40) | 8.0766e-03 | 7.9383e-03 | 4.4917e-03 | 4.2618e-03 | 2.2508e-03 | 2.0460e-03 |
| (33,10,82) | 6.7691e-03 | 1.2061e-02 | 3.4710e-03 | 9.7303e-03 | 1.6353e-03 | 3.6611e-03 |
| (46,20,113) | 5.7542e-03 | 4.7375e-03 | 2.7277e-03 | 1.6355e-03 | 1.1689e-03 | 5.6815e-04 |

**Table 5.** RMS and $L^2$ errors for Example 4.1 with the algebraically decaying solution using the Matern kernel when $t = 1$ with $\tau = 1/1024$.

| $(N_I, N_B, N_E)$ | $\gamma = 1.2$ | | | $\gamma = 1.5$ | | | $\gamma = 1.8$ | | |
|---|---|---|---|---|---|---|---|---|---|
| | $\|e\|_{rms}$ | cond($M$) | $\eta$ | $\|e\|_{rms}$ | cond($M$) | $\eta$ | $\|e\|_{rms}$ | cond($M$) | $\eta$ |
| (17,10,40) | 4.3333e-04 | 7.70e+06 | 1.00 | 2.4142e-04 | 7.70e+06 | 1.01 | 1.2055e-04 | 7.76e+06 | 1.01 |
| (33,10,82) | 3.8585e-04 | 8.95e+08 | 1.00 | 1.9567e-04 | 8.95e+08 | 1.01 | 9.1252e-05 | 8.98e+08 | 1.01 |
| (46,20,113) | 3.2339e-04 | 1.60e+10 | 1.00 | 1.5116e-04 | 1.60e+10 | 1.01 | 6.3859e-05 | 1.61e+10 | 1.01 |
| | $\|e\|_I$ | | | $\|e\|_I$ | | | $\|e\|_I$ | | |
| (17,10,40) | 5.1800e-04 | | | 2.8757e-04 | | | 1.4307e-04 | | |
| (33,10,82) | 4.2437e-04 | | | 2.1486e-04 | | | 9.9701e-05 | | |
| (46,20,113) | 3.5887e-04 | | | 1.6736e-04 | | | 6.9963e-05 | | |

We also plot the errors on a base-10 logarithmic scale against $\log_{10}(N_t)$, the logarithm of the number of time subintervals, in Figures 2 and 3. For both cases where the exact solutions are algebraically and exponentially decaying, the convergence rates are close to 1 using both Matern and Gaussian kernels. To further validate temporal convergence, we plot the convergence of the $L^2$ errors for algebraically decaying solutions using Matern and Gaussian kernels in Figure 4, and observe behavior similar to the RMS errors in Figure 2.

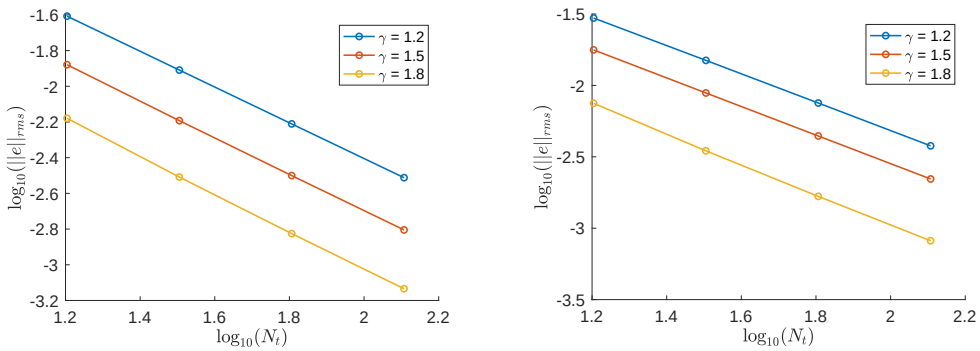


**Figure 2.** Convergence rates with respect to time in RMS errors for the algebraically decaying solution using Matern (left) and Gaussian (right) kernels when $(N_I, N_B, N_E) = (33, 10, 82)$ for Example 4.1.

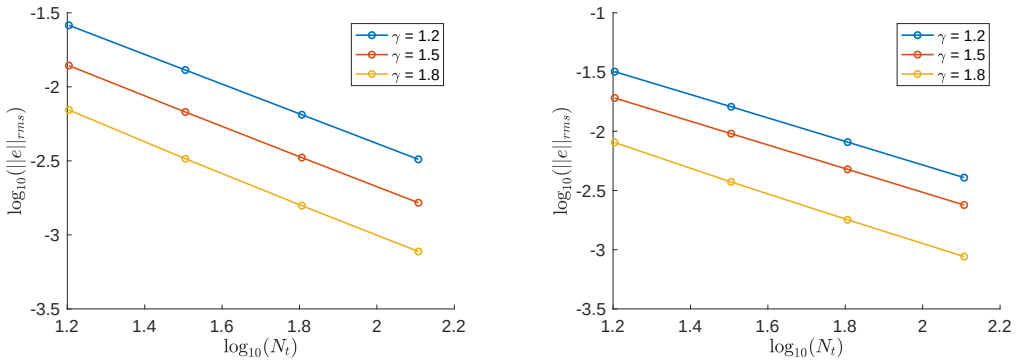


**Figure 3.** Convergence rates with respect to time in RMS errors for the exponentially decaying solution using Matern (left) and Gaussian (right) kernels when $(N_I, N_B, N_E) = (33, 10, 82)$ for Example 4.1.

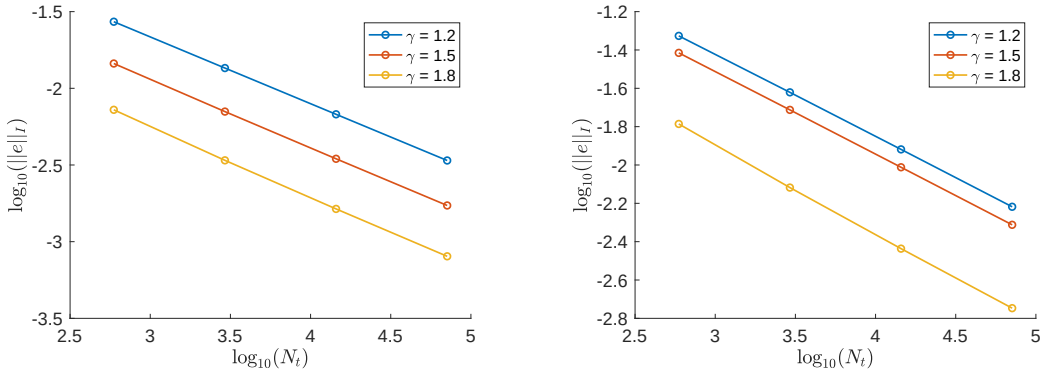


**Figure 4.** Convergence rates with respect to time in $L^2$ errors for the algebraically decaying solution using Matern (left) and Gaussian (right) kernels when $(N_I, N_B, N_E) = (33, 10, 82)$ for Example 4.1.

**Example 4.2** (Fractional heat equation, 3/4 unit disk domain)**.** In this example, we test for the exponentially decaying solution and the compactly supported solution. The domain considered is $\Omega = \{(x, y) \,|\, x = \cos\theta, y = \sin\theta, 0 < \theta < \frac{3\pi}{2}\}$. We select the extended domain to be $\widetilde{\Omega} = \{(x, y)|x^2 + y^2 < (1 + \epsilon_0)^2\}$, with $\epsilon_0 = 0.1$.

We generate the collocation points in Figure 5 in the following manner: We begin by generating a Halton sequence of points within the square $[-1, 1]^2$, which are then mapped to the unit disk $\{(x, y) \mid x^2 + y^2 < 1\}$ using the elliptical grid transformation. Then, by eliminating the points too close to $\partial\Omega$, we obtain $X_I$ and one part of $X_E$ contained in the lower-right quarter circle. We may enrich $X_E$ with uniformly distributed collocation points inside the 3/4 annulus, as shown in Figure 5 (right). We employ points that are uniformly distributed along $\partial\Omega$.

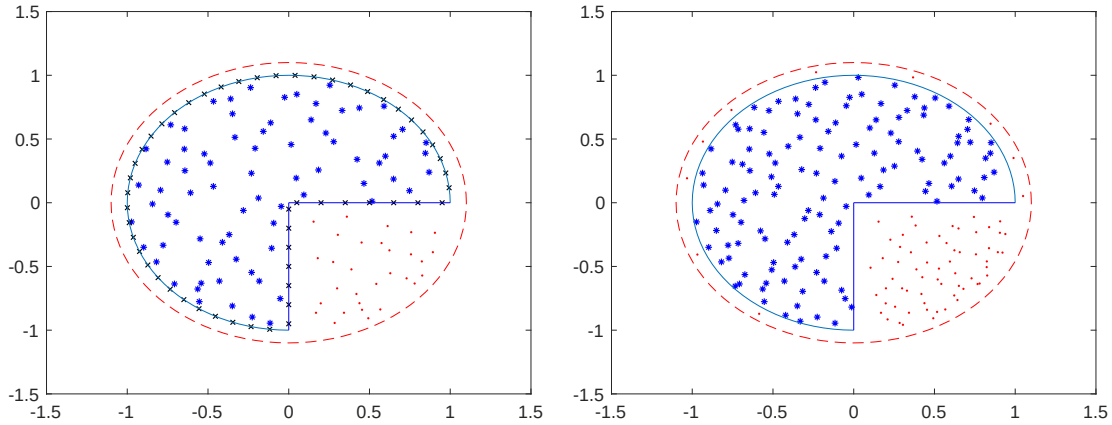


**Figure 5.** Sketch of 3/4 unit disk and the extended domain $\widetilde{\Omega}$. The blue solid curve denotes the boundary $\partial\Omega$, while the red dashed curve indicates the extended boundary $\partial\widetilde{\Omega}$. Interior collocation points are marked by blue "$*$", boundary points by black "$\times$", and collocation points in the band $\widetilde{\Omega} \setminus \overline{\Omega}$ by red "$\cdot$". Left: scattering exterior points only in the sector; Right: also scattering some points in the 3/4 annulus.

To further examine the impact of collocation point distribution on stability, as learned from Example 4.1, interior points should not be placed too close to the boundary. This consideration naturally extends to exterior points as well. As shown in Table 6, comparing the cases $(N_I, N_B, N_E) = (58, 23, 23)$ and $(58, 23, 24)$ (corresponding to the left and right parts of Figure 6, respectively), we observe that when the point distribution remains nearly identical, placing an exterior collocation point closer to $\partial\Omega$ can significantly exacerbate stability issues. Therefore, from our study on the distribution of collocation points in Examples 4.1 and 4.2, supported by extensive numerical experiments and our previous pertinent discussion regarding the point placement in Figures 1 and 5, we observe that, for a stable first-order time-dependent scheme, it is crucial to *avoid placing interior and exterior points too close to the boundary*.

**Table 6.** Points distance comparison and resulting $\eta$ using the Gaussian kernel with $\gamma = 1.8, \tau = 1/64$ for Example 4.2.

| $(N_I, N_B, N_E)$ | minAll | min IB | min E | min BE | min Ic | min Ec | $\eta$ |
|---|---|---|---|---|---|---|---|
| (53,23,23) | 0.051 | 0.051 | 0.055 | 0.055 | 0.093 | 0.056 | 1.07 |
| (53,23,24) | 0.044 | 0.051 | 0.055 | 0.044 | 0.093 | 0.036 | 0.98 |
| (114,23,43) | 0.046 | 0.049 | 0.046 | 0.046 | 0.093 | 0.065 | 0.53 |

Moreover, using an excessive number of collocation points should be avoided, as it can lead to very large condition numbers, particularly when using the Gaussian kernel (as discussed in Example 4.1), thereby compromising stability (see, e.g., the last line of Table 6). Based on the investigation of point distances and conditioning in Examples 4.1 and 4.2, we propose a *rule of thumb for collocation points*, as outlined in Remark 4.1.

We collect the results for solving the fractional heat conduction equation with the Matern kernel

when the exact solution is compactly supported in Table 7; while using the Gaussian kernel when the exact solution is exponentially decaying in Table 11. For these numerical tests, the points are collocated with the style in Figure 5 (right). In both cases, the numerical solutions match the exact solutions reasonably well. In contrast, if we do not use an extended domain, i.e., $\widetilde{\Omega} = \overline{\Omega}$ in (2.9), the results are summarized in Tables 9 and 12. Comparing Tables 7 and 9, as well as Tables 11 and 12, we observe that, when using the same interior and boundary collocation points, incorporating an extended domain and exterior collocation points generally enhances accuracy while maintaining comparable conditioning. This improvement is particularly evident for the Gaussian kernel when the number of collocation points is relatively large, as highlighted in the last line of Tables 11 and 12.

On the other hand, we also test the case where $N_B + N_E$ equals $N_B$ from the scheme without an extended domain. The corresponding results are presented in Tables 10 and 13. For these additional tests, the points $X_E$ follow the style shown in Figure 5 (right). To facilitate specifying the required number of exterior points, we generate points in the lower quarter circle with $\theta$ uniformly distributed and $r$ sampled using the Halton sequence. As observed from the comparison between Tables 9 and 10, as well as Tables 12 and 13, the scheme with an extended domain provides at least comparable accuracy and conditioning for the same total number of collocation points. We also record the corresponding $L^2$ error in Table 14. It further demonstrates that, for fixed $N_I$, when $N_B + N_E$ in Formulation II equals $N_B$ in Formulation I, Formulation II achieves comparable (or better) accuracy. Notably, when using the Gaussian kernel with $N_I = 56$, introducing the extended domain and exterior collocation points reduces the condition number by *at least four orders of magnitude* while also improving accuracy, as highlighted in Tables 12 (Row 2) and 13 (Row 1). These observations suggest that the scheme with an extended domain allows partial redistribution of collocation points into the exterior domain, thereby improving conditioning and accuracy. The reduced collocation point density achieved through the extended domain also helps to enhance the stability in time evolution.

To examine spatial convergence for the first-order scheme, a small time step of $\tau = 1/1024$ is used. The results, obtained in both RMS and $L^2$ errors for a compactly supported solution with the Matern kernel and shown in Table 8, demonstrate spatial convergence as the number of collocation points increases. As for the temporal convergence, we plot the errors in log scale ($\log_{10}$) versus time interval partition $N_t$ in Figure 7 (in RMS errors) and Figure 8 (in $L^2$ errors). We observe that when the exact solution is compactly supported and the Matern kernel is used, and when the solution is exponentially decaying and the Gaussian kernel is applied, the convergence rates are approximately 1.

**Remark 4.1** (A rule of thumb for collocation points)**.** For RBF collocation methods for fractional heat problems, stability tends to be preserved when collocation points are neither overly dense nor placed too close to the domain boundary. Based on extensive numerical experiments for the first-order time-discrete scheme, the recommended distance from an interior/exterior collocation point $\mathbf{x}$ to the boundary is $dist(\mathbf{x}, \partial\Omega) \geq 0.05 \times 10^{[\log_{10} r]}$, with $r$ the radius of the smallest disk that encloses $\Omega$ and $[\cdot]$ the floor function. This rule may also apply to other time-dependent fractional problems.

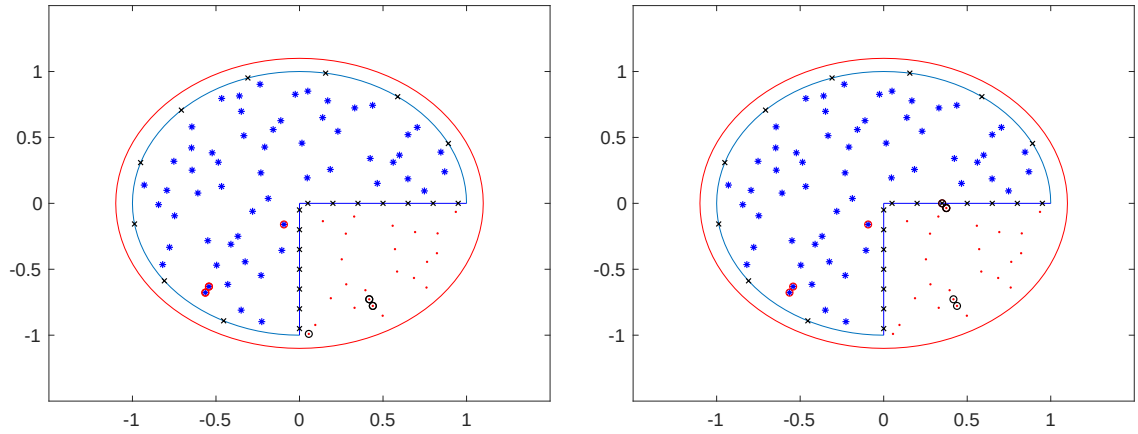


**Figure 6.** Left: $(N_I, N_B, N_E) = (58, 23, 23)$; Right : $(N_I, N_B, N_E) = (58, 23, 24)$.

**Table 7.** RMS errors for Example 4.2 with the compactly supported solution using the Matern kernel when $t = 1$, with $\tau = 1/64$.

| $(N_I, N_B, N_E)$ | $\gamma = 1.2$ | | | $\gamma = 1.5$ | | | $\gamma = 1.8$ | | |
|---|---|---|---|---|---|---|---|---|---|
| | $\|\|e\|\|_{rms}$ | cond$(M)$ | $\eta$ | $\|\|e\|\|_{rms}$ | cond$(M)$ | $\eta$ | $\|\|e\|\|_{rms}$ | cond$(M)$ | $\eta$ |
| (29,33,16) | 1.8627e-03 | 3.99e+07 | 1.05 | 5.6569e-04 | 3.97e+07 | 1.08 | 4.4391e-04 | 3.93e+07 | 1.12 |
| (56,53,29) | 2.4052e-03 | 1.31e+09 | 1.06 | 1.2977e-03 | 1.29e+09 | 1.09 | 6.1218e-04 | 1.26e+09 | 1.14 |
| (85,53,40) | 2.5710e-03 | 2.25e+09 | 1.06 | 1.3688e-03 | 2.20e+09 | 1.09 | 6.0957e-04 | 2.14e+09 | 1.14 |

**Table 8.** RMS and $L^2$ errors for Example 4.2 with the compactly supported solution using the Matern kernel when $t = 1$, with $\tau = 1/1024$.

| $(N_I, N_B, N_E)$ | $\gamma = 1.2$ | | | $\gamma = 1.5$ | | | $\gamma = 1.8$ | | |
|---|---|---|---|---|---|---|---|---|---|
| | $\|\|e\|\|_{rms}$ | cond$(M)$ | $\eta$ | $\|\|e\|\|_{rms}$ | cond$(M)$ | $\eta$ | $\|\|e\|\|_{rms}$ | cond$(M)$ | $\eta$ |
| (29,33,16) | 6.9858e-04 | 3.97e+07 | 1.00 | 9.8739e-04 | 3.97e+07 | 1.01 | 1.1279e-03 | 3.96e+07 | 1.01 |
| (56,53,29) | 2.0417e-04 | 1.32e+09 | 1.00 | 1.4785e-04 | 1.32e+09 | 1.01 | 9.4838e-05 | 1.31e+09 | 1.01 |
| (85,53,40) | 1.8127e-04 | 2.29e+09 | 1.00 | 9.7184e-05 | 2.27e+09 | 1.01 | 4.1399e-05 | 2.24e+09 | 1.01 |
| | $\|\|e\|\|_I$ | | | $\|\|e\|\|_I$ | | | $\|\|e\|\|_I$ | | |
| (29,33,16) | 1.1634e-03 | | | 1.5644e-03 | | | 1.7564e-03 | | |
| (56,53,29) | 3.0515e-04 | | | 2.1874e-04 | | | 1.3998e-04 | | |
| (85,53,40) | 2.5873e-04 | | | 1.3645e-04 | | | 5.8536e-05 | | |

**Table 9.** RMS errors for Example 4.2 with the compactly supported solution using the Matern kernel when $t = 1$, with $\tau = 1/64$, *without an extended domain (Formulation I).*

| $(N_I, N_B)$ | $\gamma = 1.2$ | | | $\gamma = 1.5$ | | | $\gamma = 1.8$ | | |
|---|---|---|---|---|---|---|---|---|---|
| | $\|e\|_{rms}$ | cond$(M)$ | $\eta$ | $\|e\|_{rms}$ | cond$(M)$ | $\eta$ | $\|e\|_{rms}$ | cond$(M)$ | $\eta$ |
| (29,33) | 1.5738e-03 | 2.99e+07 | 1.06 | 4.9517e-04 | 3.00e+07 | 1.08 | 6.7644e-04 | 2.98e+07 | 1.13 |
| (56,53) | 2.5817e-03 | 9.04e+08 | 1.06 | 1.3812e-03 | 9.11e+08 | 1.09 | 6.2088e-04 | 9.11e+08 | 1.14 |
| (85,53) | 2.7128e-03 | 1.23e+09 | 1.06 | 1.4618e-03 | 1.24e+09 | 1.09 | 6.6468e-04 | 1.24e+09 | 1.14 |

**Table 10.** RMS errors for Example 4.2 with the compactly supported solution using the Matern kernel when $t = 1$, with $\tau = 1/64$. Here $N_B + N_E$ equals $N_B$ in Table 9.

| $(N_I, N_B, N_E)$ | $\gamma = 1.2$ | | | $\gamma = 1.5$ | | | $\gamma = 1.8$ | | |
|---|---|---|---|---|---|---|---|---|---|
| | $\|e\|_{rms}$ | cond$(M)$ | $\eta$ | $\|e\|_{rms}$ | cond$(M)$ | $\eta$ | $\|e\|_{rms}$ | cond $(M)$ | $\eta$ |
| (56,33,20) | 2.3616e-03 | 1.93e+09 | 1.06 | 1.3075e-03 | 1.93e+09 | 1.09 | 6.3215e-04 | 1.94e+09 | 1.14 |
| (85,33,20) | 2.5224e-03 | 3.01e+09 | 1.06 | 1.3717e-03 | 3.02e+09 | 1.09 | 6.2996e-04 | 3.07e+09 | 1.14 |

**Table 11.** RMS errors for Example 4.2 with the exponentially decaying solution using the Gaussian kernel when $t = 1$, with $\tau = 1/64$.

| $(N_I, N_B, N_E)$ | $\gamma = 1.2$ | | | $\gamma = 1.5$ | | | $\gamma = 1.8$ | | |
|---|---|---|---|---|---|---|---|---|---|
| | $\|e\|_{rms}$ | cond$(M)$ | $\eta$ | $\|e\|_{rms}$ | cond$(M)$ | $\eta$ | $\|e\|_{rms}$ | cond$(M)$ | $\eta$ |
| (29,33,16) | 6.2746e-03 | 4.09e+09 | 1.06 | 3.9903e-03 | 3.98e+09 | 1.08 | 2.3140e-03 | 3.79e+09 | 1.12 |
| (56,53,29) | 5.4843e-03 | 4.59e+17 | 1.07 | 4.0712e-03 | 1.17e+17 | 1.10 | 4.0248e-03 | 9.13e+16 | 1.14 |
| (85,53,40) | **3.5905e-03** | 1.42e+17 | 1.08 | **1.7009e-03** | 7.88e+16 | 1.12 | **8.6051e-04** | 2.71e+17 | 1.17 |

**Table 12.** RMS errors for Example 4.2 with the exponentially decaying solution using the Gaussian kernel when $t = 1$, with $\tau = 1/64$, *without an extended domain (Formulation I).*

| $(N_I, N_B)$ | $\gamma = 1.2$ | | | $\gamma = 1.5$ | | | $\gamma = 1.8$ | | |
|---|---|---|---|---|---|---|---|---|---|
| | $\|e\|_{rms}$ | cond$(M)$ | $\eta$ | $\|e\|_{rms}$ | cond$(M)$ | $\eta$ | $\|e\|_{rms}$ | cond$(M)$ | $\eta$ |
| (29,33) | 5.4996e-03 | 2.05e+09 | 1.06 | 2.8687e-03 | 2.02e+09 | 1.10 | 1.2860e-03 | 1.94e+09 | 1.16 |
| (56,53) | **5.9306e-03** | **1.18e+17** | 1.06 | **3.5522e-03** | **1.01e+17** | 1.09 | **1.8912e-03** | **6.79e+17** | 1.13 |
| (85,53) | **6.6639e-03** | 6.78e+16 | 1.06 | **3.9613e-03** | 6.91e+16 | 1.09 | **2.0260e-03** | 5.80e+17 | 1.13 |

**Table 13.** RMS errors for Example 4.2 with the exponentially decaying solution using the Gaussian kernel when $t = 1$, with $\tau = 1/64$. Here $N_B + N_E$ equals $N_B$ in Table 12.

| $(N_I, N_B, N_E)$ | $\gamma = 1.2$ | | | $\gamma = 1.5$ | | | $\gamma = 1.8$ | | |
|---|---|---|---|---|---|---|---|---|---|
| | $\|e\|_{rms}$ | cond$(M)$ | $\eta$ | $\|e\|_{rms}$ | cond$(M)$ | $\eta$ | $\|e\|_{rms}$ | cond$(M)$ | $\eta$ |
| (56,33,20) | **3.5033e-03** | **1.11e+13** | 1.07 | **2.0409e-03** | **9.89e+12** | 1.10 | **1.1653e-03** | **8.18e+12** | 1.15 |
| (85,33,20) | 4.2221e-03 | 5.52e+14 | 1.07 | 2.3170e-03 | 4.64e+14 | 1.10 | 1.3606e-03 | 4.28e+14 | 1.15 |

**Table 14.** $L^2$ errors for Example 4.2 with the exponentially decaying solution using the Gaussian kernel when $t = 1$, with $\tau = 1/64$ using Formulations I and II. Here, for a given $N_I$, $N_B + N_E$ in Formulation II equals $N_B$ in Formulation I.

| $(N_I, N_B)$ or $(N_I, N_B, N_E)$ | Formulation | $\gamma = 1.2$ | $\gamma = 1.5$ | $\gamma = 1.8$ |
|---|---|---|---|---|
| | | $\|\|e\|\|_I$ | $\|\|e\|\|_I$ | $\|\|e\|\|_I$ |
| (56,53) | I | 8.7957e-03 | 5.3094e-03 | 2.8717e-03 |
| (56,33,20) | II | 5.4518e-03 | 3.1300e-03 | 1.8380e-03 |
| (85,53) | I | 1.0170e-02 | 5.9555e-03 | 3.0169e-03 |
| (85,33,20) | II | 1.4451e-02 | 6.4262e-03 | 2.7422e-03 |

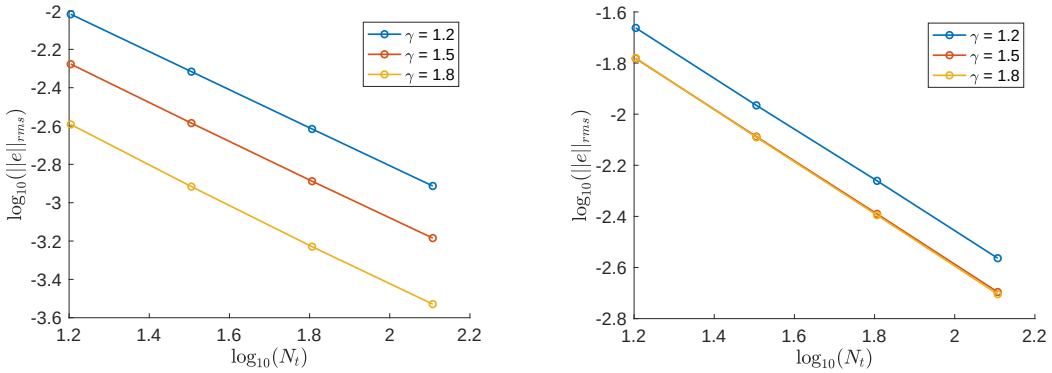


**Figure 7.** Convergence rates with respect to time in RMS errors for the compactly supported solution using the Matern kernel (left) and the exponentially decaying (right) solution using the Gaussian kernel when $(N_I, N_B, N_E) = (56, 53, 29)$ for Example 4.2.

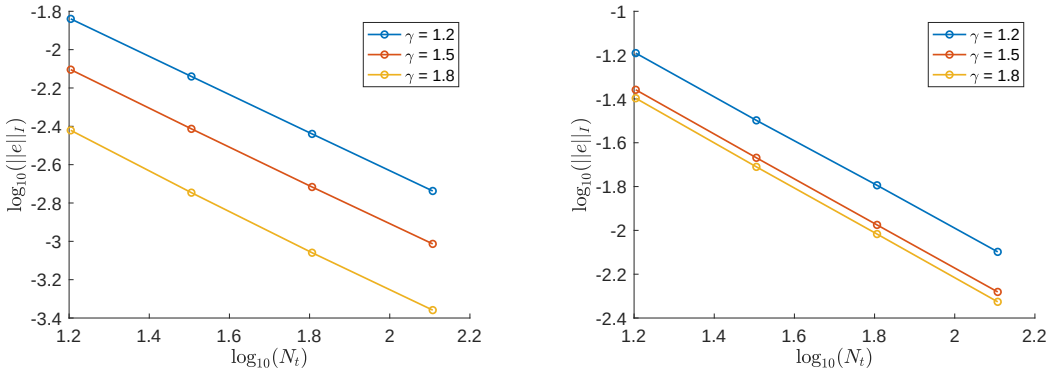


**Figure 8.** Convergence rates with respect to time in $L^2$ errors for the compactly supported solution using the Matern kernel (left) and exponentially decaying (right) solution using the Gaussian kernel when $(N_I, N_B, N_E) = (56, 53, 29)$ for Example 4.2.

## 5. Numerical examples for fractional Stokes equations

In this section, we present three numerical examples for two-dimensional fractional Stokes problems: the first example considers a rotating disk with forcing, the second example focuses on a rotating 3/4 disk—a non-convex domain that provides a more challenging test case with forcing, and the third example involves a rotating 3-petal shape as a further test on another complex domain. Since the first example does not involve a complex domain, we perform with the scheme without an extended domain or exterior collocation points (i.e., $\widetilde{\Omega} = \overline{\Omega}$ in (3.8), the scheme reduces to Formulation I). For the second and third examples, we utilize the scheme with an extended domain (Formulation II) to better address the complex domains. The results generated by the scheme with (Formulation II) and without (Formulation I) an extended domain are compared in the second example.

Our focus is on the Matern kernel with $\nu = 5.5$. The RMS errors of velocity and the gradient of the pressure are respectively denoted by $\|e_{\boldsymbol{u}}\|_{rms}$ and $\|e_{\nabla p}\|_{rms}$, with the numerical solutions $\mathbf{u}_N$ and $\nabla p_N$ respectively solved from (3.24) and (3.25). We consider the time domain is $[0, T]$, with $T = 1.5$, and the time step $\tau = T/N_t$. Since the primary goal is to evaluate the collocation methods proposed in Section 3 for the *fractional model*, we focus on the case with viscosity coefficient $\nu = 1$. We also note that the conditioning of the fractional Stokes solver depends on three matrices: the RBF interpolation matrix $\Phi$ in (2.16), the Gram matrix $G$ in (3.16), and the left-hand-side matrix $M_1$ in BDF2 solver (3.24). We denote the condition number of these three matrices as cond($\Phi$), cond($G$), and cond($M_1$), respectively. The numerical stability of the BDF2 solver (3.24) that depends on the placement of collocation points is verified with Theorem 3.1, and we have found that the stability is maintained for all numerical examples presented in this section.

**Example 5.1** (Rotating disk with forcing)**.** This example considers fractional Stokes equations with an external force on a rotating unit disk $\Omega = \{(x, y)|x^2 + y^2 < 1\}$. The source term $\mathbf{f}$ is generated from (3.1) by substituting the analytical solution: $\mathbf{u} = (-y, x)^\top \exp(-(x^2 + y^2)) \sin(\pi t)$, $p = \sin(x - y + t)$. See a more detailed discussion in Appendix A.

We test the spatial convergence in Table 15, and the numerical results exhibit fast spatial convergence for $\mathbf{u}$. This becomes particularly evident with the increase in the collocation point counts from modest to modestly large, as seen in cases where $(N_I, N_B)$ increases from $(78, 20)$ to $(157, 40)$. The magnitude of the error for $\nabla p$ is relatively large; however, it still exhibits spatial convergence. Table 16 records the corresponding $L^2$ errors, which exhibit convergence behavior similar to the RMS errors in Table 15. As also demonstrated in Table 17, when the collocation point counts increase to $(N_I, N_B) = (921, 152)$, the error in $\nabla p$ decreases substantially, reaching the level of $10^{-3}$.

**Table 15.** RMS errors for Example 5.1 using the Matern kernel when $t = 1.5$, with $\tau = 1/64$.

| $(N_I, N_B)$ | $\gamma = 1.2$ | | $\gamma = 1.5$ | | $\gamma = 1.8$ | |
|---|---|---|---|---|---|---|
| | $\|e_{\mathbf{u}}\|_{rms}$ | $\|e_{\nabla p}\|_{rms}$ | $\|e_{\mathbf{u}}\|_{rms}$ | $\|e_{\nabla p}\|_{rms}$ | $\|e_{\mathbf{u}}\|_{rms}$ | $\|e_{\nabla p}\|_{rms}$ |
| (19,5) | 1.0202e-01 | 1.0722e+00 | 9.9776e-02 | 1.0528e+00 | 1.0496e-01 | 1.0439e+00 |
| (39,10) | 6.1334e-02 | 9.8100e-01 | 5.6273e-02 | 1.0245e+00 | 5.1998e-02 | 1.1369e+00 |
| (78,20) | 2.0796e-02 | 7.9162e-01 | 1.9256e-02 | 8.0146e-01 | 1.6988e-02 | 8.2331e-01 |
| (157,40) | 1.1227e-03 | 2.5972e-01 | 1.0845e-03 | 2.7266e-01 | 1.0458e-03 | 3.0901e-01 |

**Table 16.** $L^2$ errors for Example 5.1 using the Matern kernel when $t = 1.5$, with $\tau = 1/64$.

| $(N_I, N_B)$ | $\gamma = 1.2$ | | $\gamma = 1.5$ | | $\gamma = 1.8$ | |
|---|---|---|---|---|---|---|
| | $\|\|e_{\mathbf{u}}\|\|_I$ | $\|\|e_{\nabla p}\|\|_I$ | $\|\|e_{\mathbf{u}}\|\|_I$ | $\|\|e_{\nabla p}\|\|_I$ | $\|\|e_{\mathbf{u}}\|\|_I$ | $\|\|e_{\nabla p}\|\|_I$ |
| (19,5) | 1.9818e-01 | 1.6332e+00 | 1.9754e-01 | 1.6256e+00 | 2.0892e-01 | 1.6271e+00 |
| (39,10) | 1.1302e-01 | 1.7734e+00 | 1.0382e-01 | 1.8251e+00 | 9.5917e-02 | 1.9584e+00 |
| (78,20) | 3.8133e-02 | 1.4424e+00 | 3.5354e-02 | 1.4580e+00 | 3.1252e-02 | 1.4892e+00 |
| (157,40) | 2.4775e-03 | 5.0986e-01 | 2.4028e-03 | 5.4461e-01 | 2.3332e-03 | 6.4079e-01 |

We also examine the temporal convergence in Table 17, with $(N_I, N_B) = (921, 152)$. The table indicates the fast temporal convergence for $\mathbf{u}$. Furthermore, when the time division is moderately fine, the solution accuracy for $\mathbf{u}$ is very high (e.g., reaching the level of $10^{-6}$ when $\tau = 1/64$). We note that $\nabla p$ does not exhibit clear temporal convergence. This is likely because the current reconstruction of $\nabla p$ from (3.22) is a relatively simplified approximation, where the spatial errors may dominate. Table 18 records the corresponding $L^2$ errors, which exhibit convergence behavior similar to the RMS errors in Table 17. Utilizing the Matern kernel, the solver remains well-conditioned. Even in the case of larger number of collocation points $(N_I, N_B) = (921, 152)$, cond($\Phi$) and cond($G$) are within the level of $10^{11}$, and cond($M_1$) is within the level $10^1$.

**Table 17.** RMS errors for Example 5.1 using the Matern kernel when $t = 1.5$ under different time divisions $N_t$, with $(N_I, N_B) = (921, 152)$ using the divergence free kernel method.

| $N_t$ | $\gamma = 1.2$ | | $\gamma = 1.5$ | | $\gamma = 1.8$ | |
|---|---|---|---|---|---|---|
| | $\|\|e_{\mathbf{u}}\|\|_{rms}$ | $\|\|e_{\nabla p}\|\|_{rms}$ | $\|\|e_{\mathbf{u}}\|\|_{rms}$ | $\|\|e_{\nabla p}\|\|_{rms}$ | $\|\|e_{\mathbf{u}}\|\|_{rms}$ | $\|\|e_{\nabla p}\|\|_{rms}$ |
| 6 | 6.6208e-03 | 3.2253e-03 | 5.8126e-03 | 4.1787e-03 | 4.8221e-03 | 4.7639e-03 |
| 12 | 1.1061e-03 | 2.7437e-03 | 9.5248e-04 | 2.9709e-03 | 7.7098e-04 | 3.5799e-03 |
| 24 | 1.8819e-04 | 2.7046e-03 | 1.5862e-04 | 2.9082e-03 | 1.2462e-04 | 3.5156e-03 |
| 48 | 3.4112e-05 | 2.6986e-03 | 2.7947e-05 | 2.9013e-03 | 2.0983e-05 | 3.5078e-03 |
| 96 | 6.0924e-06 | 2.6974e-03 | 4.8701e-06 | 2.9000e-03 | 3.6329e-06 | 3.5063e-03 |
| 192 | 2.8260e-06 | 2.6972e-03 | 2.8087e-06 | 2.8997e-03 | 2.8971e-06 | 3.5060e-03 |

**Table 18.** $L^2$ errors for Example 5.1 using the Matern kernel when $t = 1.5$ under different time divisions $N_t$, with $(N_I, N_B) = (921, 152)$ using the divergence free kernel method.

| $N_t$ | $\gamma = 1.2$ | | $\gamma = 1.5$ | | $\gamma = 1.8$ | |
|---|---|---|---|---|---|---|
| | $\|\|e_{\mathbf{u}}\|\|_I$ | $\|\|e_{\nabla p}\|\|_I$ | $\|\|e_{\mathbf{u}}\|\|_I$ | $\|\|e_{\nabla p}\|\|_I$ | $\|\|e_{\mathbf{u}}\|\|_I$ | $\|\|e_{\nabla p}\|\|_I$ |
| 6 | 1.3091e-02 | 5.0486e-03 | 1.1486e-02 | 6.2716e-03 | 9.5517e-03 | 7.1985e-03 |
| 12 | 2.1992e-03 | 4.3547e-03 | 1.8920e-03 | 4.7110e-03 | 1.5346e-03 | 5.6772e-03 |
| 24 | 3.7713e-04 | 4.2826e-03 | 3.1766e-04 | 4.5883e-03 | 2.5021e-04 | 5.5513e-03 |
| 48 | 6.9570e-05 | 4.2712e-03 | 5.7097e-05 | 4.5715e-03 | 4.3177e-05 | 5.5329e-03 |
| 96 | 1.2847e-05 | 4.2691e-03 | 1.0235e-05 | 4.5684e-03 | 7.4454e-06 | 5.5294e-03 |
| 192 | 4.3724e-06 | 4.2686e-03 | 4.2848e-06 | 4.5678e-03 | 4.3427e-06 | 5.5287e-03 |

To further validate the proposed solver for the fractional Stokes equation, we perform a benchmark test against its integer-order counterpart by considering the case $\gamma = 1.999$ and comparing it with $\gamma = 2$, where the model reduces to the integer-order form. As shown in Table 19, the results for $\gamma = 1.999$ closely match those for $\gamma = 2$, further confirming the reliability and consistency of the fractional solver.

**Table 19.** RMS errors for Example 5.1 using the Matern kernel when $t = 1.5$ under different time divisions $N_t$, with $(N_I, N_B) = (921, 152)$ using the divergence-free kernel method comparing the cases where $\gamma$ is close to 2 and $\gamma = 2$.

| $N_t$ | $\gamma = 1.999$ | | $\gamma = 2$ | |
|---|---|---|---|---|
| | $\|\|e_{\mathbf{u}}\|\|_{rms}$ | $\|\|e_{\nabla p}\|\|_{rms}$ | $\|\|e_{\mathbf{u}}\|\|_{rms}$ | $\|\|e_{\nabla p}\|\|_{rms}$ |
| 6 | 4.0961e-03 | 4.5916e-03 | 4.0924e-03 | 4.5952e-03 |
| 12 | 6.4238e-04 | 4.4896e-03 | 6.4173e-04 | 4.4959e-03 |
| 24 | 1.0104e-04 | 4.4654e-03 | 1.0092e-04 | 4.4721e-03 |
| 48 | 1.6118e-05 | 4.4596e-03 | 1.6093e-05 | 4.4663e-03 |
| 96 | 3.0351e-06 | 4.4581e-03 | 3.0335e-06 | 4.4649e-03 |
| 192 | 3.2469e-06 | 4.4578e-03 | 3.2501e-06 | 4.4645e-03 |

**Example 5.2** (Rotating 3/4 disk with forcing)**.** This example considers fractional Stokes equations with an external force on a spinning 3/4 unit disk $\Omega = \left\{(x, y) \,\middle|\, x = \cos\theta, y = \sin\theta, 0 < \theta < \frac{3\pi}{2}\right\}$. The source term $\mathbf{f}$ is generated from (3.1) with the following analytical solution: $\mathbf{u} = (-y, x)^\top \exp(-(x^2+y^2)) \sin(\pi t)$ and $p = \sin(x - y + t)$. We select the extended domain as $\widetilde{\Omega} = \{(x, y)|x^2 + y^2 < (1 + \epsilon_0)^2\}$, with $\epsilon_0 = 0.1$.

The strategy to deploy the collocation points is the same in Example 4.2. We present the spatial convergence results for the scheme with the extended domain (Formulation II) in Tables 20 and 21, and compare the temporal convergence results of Formulations I and II in Tables 22 and 23 in RMS errors, and in Tables 24 and 25 in $L^2$ errors, respectively. Tables 20 and 21 indicate that the results with Formulation II in general exhibit fast spatial convergence and provide a good approximation when a modestly large number of collocation points are employed.

The comparison of Tables 22 (Formulation I) and 23 (Formulation II) indicates that introducing the extended domain and placing collocation points in the exterior region can significantly improve accuracy. In particular, as highlighted in the tables, when $\tau$ is moderately small ($\tau = 1/64$), the error for $\mathbf{u}$ using Formulation II is reduced by over 90% compared to that of Formulation I. The corresponding $L^2$ errors in Tables 24 (Formulation I) and 25 (Formulation II) exhibit similar behaviors. Under the BDF2 scheme, the conditioning of the solvers for both formulations remains comparable: cond($\Phi$) and cond($G$) are within the order of $10^{12}$, and cond($M_1$) is within $10^5$. The results with Formulation II also demonstrate faster temporal convergence compared to Formulation I. For Formulation II, temporal convergence for $\mathbf{u}$ is observed with respect to a time subdivision up to $N_t = 192$, although the convergence rates become small for $N_t > 48$. In contrast, for Formulation I, no temporal convergence for $\mathbf{u}$ is observed once $N_t > 24$.

**Table 20.** RMS errors for Example 5.2 using the Matern kernel when $t = 1.5$, with $\tau = 1/64$.

| $(N_I, N_B, N_E)$ | $\gamma = 1.2$ | | $\gamma = 1.5$ | | $\gamma = 1.8$ | |
|---|---|---|---|---|---|---|
| | $\|\|e_{\mathbf{u}}\|\|_{rms}$ | $\|\|e_{\nabla p}\|\|_{rms}$ | $\|\|e_{\mathbf{u}}\|\|_{rms}$ | $\|\|e_{\nabla p}\|\|_{rms}$ | $\|\|e_{\mathbf{u}}\|\|_{rms}$ | $\|\|e_{\nabla p}\|\|_{rms}$ |
| (69,16,30) | 1.9344e-02 | 6.9240e-01 | 1.7896e-02 | 7.1516e-01 | 1.5837e-02 | 7.6635e-01 |
| (135,32,59) | 4.6843e-03 | 3.1351e-01 | 4.4092e-03 | 3.2924e-01 | 3.9424e-03 | 3.5987e-01 |
| (271,63,118) | 6.3254e-05 | 2.3585e-02 | 6.1549e-05 | 2.5134e-02 | 5.8829e-05 | 2.8995e-02 |
| (546,128,232) | 5.1719e-05 | 9.4610e-03 | 5.0511e-05 | 1.0271e-02 | 4.8616e-05 | 1.2293e-02 |

**Table 21.** $L^2$ errors for Example 5.2 using the Matern kernel when $t = 1.5$, with $\tau = 1/64$.

| $(N_I, N_B, N_E)$ | $\gamma = 1.2$ | | $\gamma = 1.5$ | | $\gamma = 1.8$ | |
|---|---|---|---|---|---|---|
| | $\|\|e_{\mathbf{u}}\|\|_I$ | $\|\|e_{\nabla p}\|\|_I$ | $\|\|e_{\mathbf{u}}\|\|_I$ | $\|\|e_{\nabla p}\|\|_I$ | $\|\|e_{\mathbf{u}}\|\|_I$ | $\|\|e_{\nabla p}\|\|_I$ |
| (69,16,30) | 2.8420e-02 | 8.9533e-01 | 2.6292e-02 | 9.2068e-01 | 2.3277e-02 | 9.8543e-01 |
| (135,32,59) | 6.5091e-03 | 4.0279e-01 | 6.1266e-03 | 4.2195e-01 | 5.4783e-03 | 4.5873e-01 |
| (271,63,118) | 8.6617e-05 | 3.7084e-02 | 8.4231e-05 | 3.9028e-02 | 8.0553e-05 | 4.3861e-02 |
| (546,128,232) | 8.7551e-05 | 1.6150e-02 | 8.5443e-05 | 1.7452e-02 | 8.1734e-05 | 2.0492e-02 |

**Table 22.** RMS errors for Example 5.2 using the Matern kernel when $t = 1.5$ under different time divisions $N_t$, with Formulation I: $(N_I, N_B) = (1112, 172)$.

| $N_t$ | $\gamma = 1.2$ | | $\gamma = 1.5$ | | $\gamma = 1.8$ | |
|---|---|---|---|---|---|---|
| | $\|\|e_{\mathbf{u}}\|\|_{rms}$ | $\|\|e_{\nabla p}\|\|_{rms}$ | $\|\|e_{\mathbf{u}}\|\|_{rms}$ | $\|\|e_{\nabla p}\|\|_{rms}$ | $\|\|e_{\mathbf{u}}\|\|_{rms}$ | $\|\|e_{\nabla p}\|\|_{rms}$ |
| 6 | 1.3667e-03 | 1.0767e-01 | 1.1944e-03 | 1.0790e-01 | 9.6088e-04 | 1.0878e-01 |
| 12 | 1.8902e-04 | 1.9350e-02 | 1.6822e-04 | 2.0030e-02 | 1.4524e-04 | 2.1772e-02 |
| 24 | 1.3809e-04 | 9.4355e-03 | 1.3845e-04 | 1.0349e-02 | 1.4135e-04 | 1.2642e-02 |
| 48 | 1.5162e-04 | 8.6118e-03 | 1.5083e-04 | 9.5396e-03 | 1.5206e-04 | 1.1880e-02 |
| 96 | **1.5443e-04** | 8.5272e-03 | **1.5333e-04** | 9.4560e-03 | **1.5414e-04** | 1.1801e-02 |
| 192 | 1.5500e-04 | 8.5181e-03 | 1.5382e-04 | 9.4472e-03 | 1.5455e-04 | 1.1793e-02 |

**Table 23.** RMS errors for Example 5.2 using the Matern kernel when $t = 1.5$ under different time divisions $N_t$, with Formulation II: $(N_I, N_B, N_E) = (1112, 172, 443)$.

| $N_t$ | $\gamma = 1.2$ | | $\gamma = 1.5$ | | $\gamma = 1.8$ | |
|---|---|---|---|---|---|---|
| | $\|\|e_{\mathbf{u}}\|\|_{rms}$ | $\|\|e_{\nabla p}\|\|_{rms}$ | $\|\|e_{\mathbf{u}}\|\|_{rms}$ | $\|\|e_{\nabla p}\|\|_{rms}$ | $\|\|e_{\mathbf{u}}\|\|_{rms}$ | $\|\|e_{\nabla p}\|\|_{rms}$ |
| 6 | 1.2622e-03 | 1.0953e-01 | 1.1070e-03 | 1.0940e-01 | 8.9648e-04 | 1.0946e-01 |
| 12 | 1.9509e-04 | 1.5043e-02 | 1.7017e-04 | 1.5050e-02 | 1.3701e-04 | 1.5143e-02 |
| 24 | 3.6087e-05 | 3.2399e-03 | 3.2022e-05 | 3.4480e-03 | 2.6710e-05 | 4.0182e-03 |
| 48 | 1.4490e-05 | 2.6898e-03 | 1.3734e-05 | 2.9439e-03 | 1.2689e-05 | 3.6132e-03 |
| 96 | **1.1790e-05** | 2.6843e-03 | **1.1489e-05** | 2.9385e-03 | **1.1007e-05** | 3.6094e-03 |
| 192 | 1.1364e-05 | 2.6837e-03 | 1.1135e-05 | 2.9377e-03 | 1.0741e-05 | 3.6086e-03 |

**Table 24.** $L^2$ errors for Example 5.2 using the Matern kernel when $t = 1.5$ under different time divisions $N_t$, with Formulation I: $(N_I, N_B) = (1112, 172)$.

| $N_t$ | $\gamma = 1.2$ | | $\gamma = 1.5$ | | $\gamma = 1.8$ | |
|---|---|---|---|---|---|---|
| | $\|e_{\mathbf{u}}\|_I$ | $\|e_{\nabla p}\|_I$ | $\|e_{\mathbf{u}}\|_I$ | $\|e_{\nabla p}\|_I$ | $\|e_{\mathbf{u}}\|_I$ | $\|e_{\nabla p}\|_I$ |
| 6 | 2.1105e-03 | 1.9038e-01 | 1.8461e-03 | 1.9093e-01 | 1.4895e-03 | 1.9323e-01 |
| 12 | 3.3493e-04 | 4.7802e-02 | 3.0345e-04 | 5.0896e-02 | 2.6787e-04 | 6.0356e-02 |
| 24 | 2.4187e-04 | 3.9886e-02 | 2.4113e-04 | 4.3363e-02 | 2.4334e-04 | 5.3986e-02 |
| 48 | 2.5561e-04 | 3.9546e-02 | 2.5409e-04 | 4.3005e-02 | 2.5507e-04 | 5.3630e-02 |
| 96 | 2.5883e-04 | 3.9497e-02 | 2.5699e-04 | 4.2951e-02 | 2.5756e-04 | 5.3569e-02 |
| 192 | 2.5951e-04 | 3.9486e-02 | 2.5759e-04 | 4.2939e-02 | 2.5807e-04 | 5.3555e-02 |

**Table 25.** $L^2$ errors for Example 5.2 using the Matern kernel when $t = 1.5$ under different time divisions $N_t$, with Formulation II: $(N_I, N_B, N_E) = (1112, 172, 443)$.

| $N_t$ | $\gamma = 1.2$ | | $\gamma = 1.5$ | | $\gamma = 1.8$ | |
|---|---|---|---|---|---|---|
| | $\|e_{\mathbf{u}}\|_I$ | $\|e_{\nabla p}\|_I$ | $\|e_{\mathbf{u}}\|_I$ | $\|e_{\nabla p}\|_I$ | $\|e_{\mathbf{u}}\|_I$ | $\|e_{\nabla p}\|_I$ |
| 6 | 1.9167e-03 | 1.8985e-01 | 1.6803e-03 | 1.8953e-01 | 1.3608e-03 | 1.8962e-01 |
| 12 | 2.9530e-04 | 2.6609e-02 | 2.5739e-04 | 2.6640e-02 | 2.0711e-04 | 2.6960e-02 |
| 24 | 5.4913e-05 | 7.5921e-03 | 4.8850e-05 | 8.1066e-03 | 4.0965e-05 | 9.5209e-03 |
| 48 | 2.4170e-05 | 6.8937e-03 | 2.3059e-05 | 7.4747e-03 | 2.1454e-05 | 9.0175e-03 |
| 96 | 2.0797e-05 | 6.8711e-03 | 2.0268e-05 | 7.4529e-03 | 1.9366e-05 | 8.9974e-03 |
| 192 | 2.0284e-05 | 6.8643e-03 | 1.9838e-05 | 7.4459e-03 | 1.9038e-05 | 8.9901e-03 |

**Example 5.3** (Rotating 3-petal shape with forcing)**.** We test with an example of the fractional Stokes problem on another complex domain. Here $\Omega = \{(r, \theta) \,|\, r < 0.7 + 0.2\sin(3\theta), 0 \le \theta < 2\pi\}$ is the same 3-petal domain as in Example 4.1. The source term $\mathbf{f}$ is generated from (3.1) with the analytical solutions $\mathbf{u}$ and $p$ the same as those in Example 5.2. The extended domain $\widetilde{\Omega}$ is selected to be a unit open disk centered at $(0, 0)$.

**Table 26.** RMS errors for Example 5.3 using the Matern kernel when $t = 1.5$, with $\tau = 1/64$.

| $(N_I, N_B, N_E)$ | $\gamma = 1.2$ | | $\gamma = 1.5$ | | $\gamma = 1.8$ | |
|---|---|---|---|---|---|---|
| | $\|e_{\mathbf{u}}\|_{rms}$ | $\|e_{\nabla p}\|_{rms}$ | $\|e_{\mathbf{u}}\|_{rms}$ | $\|e_{\nabla p}\|_{rms}$ | $\|e_{\mathbf{u}}\|_{rms}$ | $\|e_{\nabla p}\|_{rms}$ |
| (33,20,82) | 8.4967e-03 | 3.6106e-01 | 8.0170e-03 | 3.7866e-01 | 7.3149e-03 | 4.1210e-01 |
| (64,39,158) | 7.7311e-04 | 9.4833e-02 | 7.5092e-04 | 1.0062e-01 | 7.1229e-04 | 1.1303e-01 |
| (130,78,319) | 5.8190e-05 | 2.5735e-02 | 5.6081e-05 | 2.7178e-02 | 5.1758e-05 | 3.0486e-02 |
| (258,155,640) | 8.6858e-06 | 5.8476e-03 | 8.5543e-06 | 6.2260e-03 | 8.3577e-06 | 7.2700e-03 |

**Table 27.** $L^2$ errors for Example 5.3 using the Matern kernel when $t = 1.5$, with $\tau = 1/64$.

| $(N_I, N_B, N_E)$ | $\gamma = 1.2$ | | $\gamma = 1.5$ | | $\gamma = 1.8$ | |
|---|---|---|---|---|---|---|
| | $\|\|e_{\mathbf{u}}\|\|_I$ | $\|\|e_{\nabla p}\|\|_I$ | $\|\|e_{\mathbf{u}}\|\|_I$ | $\|\|e_{\nabla p}\|\|_I$ | $\|\|e_{\mathbf{u}}\|\|_I$ | $\|\|e_{\nabla p}\|\|_I$ |
| (33,20,82) | 9.7456e-03 | 4.0885e-01 | 9.1888e-03 | 4.2563e-01 | 8.3858e-03 | 4.5753e-01 |
| (64,39,158) | 8.9126e-04 | 1.2673e-01 | 8.6488e-04 | 1.3451e-01 | 8.1956e-04 | 1.5134e-01 |
| (130,78,319) | 1.0556e-04 | 5.0986e-02 | 1.0142e-04 | 5.4191e-02 | 9.2746e-05 | 6.1671e-02 |
| (258,155,640) | 1.7901e-05 | 1.0849e-02 | 1.7560e-05 | 1.1634e-02 | 1.6953e-05 | 1.3818e-02 |

**Table 28.** RMS errors for Example 5.3 using the Matern kernel when $t = 1.5$ under different time divisions $N_t$, with Formulation II: $(N_I, N_B, N_E) = (452, 291, 971)$.

| $N_t$ | $\gamma = 1.2$ | | $\gamma = 1.5$ | | $\gamma = 1.8$ | |
|---|---|---|---|---|---|---|
| | $\|\|e_{\mathbf{u}}\|\|_{rms}$ | $\|\|e_{\nabla p}\|\|_{rms}$ | $\|\|e_{\mathbf{u}}\|\|_{rms}$ | $\|\|e_{\nabla p}\|\|_{rms}$ | $\|\|e_{\mathbf{u}}\|\|_{rms}$ | $\|\|e_{\nabla p}\|\|_{rms}$ |
| 6 | 1.4974e-03 | 1.1865e-01 | 1.3149e-03 | 1.1793e-01 | 1.0615e-03 | 1.1822e-01 |
| 12 | 2.2244e-04 | 1.7161e-02 | 1.9375e-04 | 1.6973e-02 | 1.5469e-04 | 1.6932e-02 |
| 24 | 3.3085e-05 | 2.9250e-03 | 2.8478e-05 | 2.9014e-03 | 2.2353e-05 | 2.9454e-03 |
| 48 | 5.3419e-06 | 1.3506e-03 | 4.5297e-06 | 1.3927e-03 | 3.4752e-06 | 1.5249e-03 |
| 96 | 1.1638e-06 | 1.2570e-03 | 1.0216e-06 | 1.3074e-03 | 8.2846e-07 | 1.4506e-03 |
| 192 | 7.5665e-07 | 1.2512e-03 | 7.1757e-07 | 1.3022e-03 | 6.3966e-07 | 1.4464e-03 |

**Table 29.** $L^2$ errors for Example 5.3 using the Matern kernel when $t = 1.5$ under different time divisions $N_t$, with Formulation II: $(N_I, N_B, N_E) = (452, 291, 971)$.

| $N_t$ | $\gamma = 1.2$ | | $\gamma = 1.5$ | | $\gamma = 1.8$ | |
|---|---|---|---|---|---|---|
| | $\|\|e_{\mathbf{u}}\|\|_I$ | $\|\|e_{\nabla p}\|\|_I$ | $\|\|e_{\mathbf{u}}\|\|_I$ | $\|\|e_{\nabla p}\|\|_I$ | $\|\|e_{\mathbf{u}}\|\|_I$ | $\|\|e_{\nabla p}\|\|_I$ |
| 6 | 1.7702e-03 | 1.3928e-01 | 1.5544e-03 | 1.3870e-01 | 1.2552e-03 | 1.3987e-01 |
| 12 | 2.6334e-04 | 2.1404e-02 | 2.2935e-04 | 2.1182e-02 | 1.8312e-04 | 2.1217e-02 |
| 24 | 3.9227e-05 | 3.9400e-03 | 3.3757e-05 | 3.9024e-03 | 2.6489e-05 | 3.9291e-03 |
| 48 | 6.3532e-06 | 1.8293e-03 | 5.3870e-06 | 1.8548e-03 | 4.1289e-06 | 1.9175e-03 |
| 96 | 1.4860e-06 | 1.6655e-03 | 1.3153e-06 | 1.6969e-03 | 1.0705e-06 | 1.7600e-03 |
| 192 | 1.0697e-06 | 1.6486e-03 | 1.0091e-06 | 1.6801e-03 | 8.8513e-07 | 1.7423e-03 |

The strategy for deploying the collocation points is the same as in Example 4.1. The spatial convergence results are reported in Table 26 (RMS errors) and Table 27 ($L^2$ errors), while the temporal convergence results with Formulation II are given in Table 28 (RMS errors) and Table 29 ($L^2$ errors). Owing to the complexity of the domain geometry, the use of an extended domain significantly simplifies the evaluation of the exterior integrals required in (3.5) and (3.6). Similar to the observations in Example 5.2, Tables 26 and 27 demonstrate rapid spatial convergence and show that a high accuracy for $\mathbf{u}$ can be achieved with a moderately large number of collocation points. Tables 28 and 29 further confirm the effectiveness of the proposed method in achieving high accuracy and fast temporal convergence for $\mathbf{u}$. The condition numbers associated with these tests remain within reasonable scales.

For the results in Tables 26 and 27, cond($\Phi$) and cond($G$) are within the order of $10^{13}$, while cond($M_1$) is within the order of $10^2$. For the results in Tables 28 and 29, due to the denser distribution of collocation points, cond($\Phi$) increases to the order of $10^{17}$ but remains manageable; meanwhile, cond($G$) is within the order of $10^{14}$ and cond($M_1$) is within the order of $10^3$.

## 6. Conclusions and discussion

This study investigates RBF-based collocation methods for time-dependent spatial fractional problems on general bounded domains. Specifically, we consider two classes of problems: fractional heat conduction and fractional Stokes equations. The integral fractional Laplacian is evaluated using the approach developed in [24], which is based on the double exponential transformation.

The proposed collocation methods utilize extended domains, which can address problems on complex domains while improving both accuracy and conditioning compared to methods without domain extension. For fractional heat conduction problems, in addition to developing the collocation scheme, we provide a practical guideline for placing collocation points to avoid instability during time evolution. For fractional Stokes problems, the collocation method is formulated based on the Leray projection that can incorporate an extended domain to accommodate complex domains. Numerical results demonstrate that the proposed methods generally exhibit rapid spatial and temporal convergence with high accuracy.

This study presents meshless RBF methods within a pseudo-spectral framework for time-dependent nonlocal problems, demonstrating both efficiency and accuracy. Furthermore, integrating efficient numerical techniques for the integral fractional Laplacian (e.g., the approach in (1.7)), extended-domain techniques, and streamlined decoupling methods for complex PDE systems (e.g., the Leray projection for Stokes problems) offers insights for developing efficient solvers for complex fractional models on complex domains.

Future work includes solving the auxiliary problem in (3.20) and (3.21) effectively to provide a more accurate approximation for $p$. In addition, the methods developed in this study can serve as fast and good initial guesses, which can be further refined for higher precision using techniques such as spectral deferred corrections [39, 40]. Finally, we remark that the domain extension techniques, known also as immersed or fictitious domain methods [41–43], allow also a simplified numerical linear algebra for the design of preconditioners or multigrid methods; see [42, 43] and the references therein. This aspect is not discussed here, but it is worth investigating in connection with the present work.

## Appendix A. Derivation of the source term in Example 5.1

According to [15, 44], we have

$$(-\Delta)^{\frac{\gamma}{2}} \exp(-\mathbf{x}^2) = 2^{\gamma}\Gamma\left(\frac{2+\gamma}{2}\right) {}_1F_1\left(\frac{2+\gamma}{2}; 1; -|\mathbf{x}|^2\right), \quad \text{for } \mathbf{x} \in \mathbb{R}^2, \quad \gamma \geq 0.$$

We can derive the integral fractional Laplacian of the given analytical form of $\mathbf{u}$ in Example 5.1 as follows:

$$(-\Delta)^{\frac{\gamma}{2}}\mathbf{u}(\mathbf{x}, t) = 2^{\gamma}\Gamma\left(2+\frac{\gamma}{2}\right) {}_1F_1\left(2+\frac{\gamma}{2}, 2, -(x^2+y^2)\right)\sin(\pi t)\begin{bmatrix} -y \\ x \end{bmatrix}.$$

Equipped with the above identity, the source term $\mathbf{f}$ in Example 5.1 can be readily generated.

## Use of AI tools declaration

The authors declare they have not used Artificial Intelligence (AI) tools in the creation of this article.

## Acknowledgments

Yanzhi Zhang is partially supported by the US National Science Foundation DMS–1953177.

## Conflict of interest

The authors declare there are no conflicts of interest.

## References

1. K. Burrage, N. Hale, D. Kay, An efficient implicit FEM scheme for fractional-in-space reaction-diffusion equations, *SIAM J. Sci. Comput.*, **34** (2012), A2145–A2172. https://doi.org/10.1137/110847007
2. L. Vázquez, J. J. Trujillo, M. Pilar Velasco, Fractional heat equation and the second law of thermodynamics, *Fract. Calc. Appl. Anal.*, **14** (2011), 334–342. https://doi.org/10.2478/s13540-011-0021-9
3. Asifa, T. Anwar, P. Kumam, M. Y. Almusawa, S. A. Lone, P. Suttiarporn, Exact solutions via prabhakar fractional approach to investigate heat transfer and flow features of hybrid nanofluid subject to shape and slip effects, *Sci. Rep.*, **13** (2023), 7810. https://doi.org/10.1038/s41598-023-34259-9
4. M. Gunzburger, N. Jiang, F. Xu, Analysis and approximation of a fractional Laplacian-based closure model for turbulent flows and its connection to Richardson pair dispersion, *Comput. Math. Appl.*, **75** (2018), 1973–2001. https://doi.org/10.1016/j.camwa.2017.06.035
5. B. P. Epps, B. Cushman-Roisin, Turbulence modeling via the fractional Laplacian, preprint, arXiv:1803.05286.
6. S. Hittmeir, S. Merino-Aceituno, Kinetic derivation of fractional Stokes and Stokes-Fourier systems, *Kinet. Rel. Models*, **9** (2016), 105–129. https://doi.org/10.3934/krm.2016.9.105
7. S. Lin, M. Azaïez, C. Xu, A fractional Stokes equation and its spectral approximation, *Int. J. Numer. Anal. Model.*, **15** (2018), 170–192.
8. H. Wang, T. S. Basu, A fast finite difference method for two-dimensional space-fractional diffusion equations, *SIAM J. Sci. Comput.*, **34** (2012), A2444–A2458. https://doi.org/10.1137/12086491X
9. K. Sayevand, J. T. Machado, V. Moradi, A new non-standard finite difference method for analyzing the fractional Navier-Stokes equations, *Comput. Math. Appl.*, **78** (2019), 1681–1694. https://doi.org/10.1016/j.camwa.2018.12.016
10. X. Li, X. You, Mixed finite element methods for fractional Navier-Stokes equations, *J. Comput. Math.*, **39** (2021), 130–146. https://doi.org/10.4208/jcm.1911-m2018-0153

11. Y. Jiao, T. Li, Z. Zhang, Jacobi spectral collocation method of space-fractional Navier-Stokes equations, *Appl. Math. Comput.*, **488** (2025), 129111. https://doi.org/10.1016/j.amc.2024.129111
12. A. Bueno-Orovio, D. Kay, K. Burrage, Fourier spectral methods for fractional-in-space reaction-diffusion equations, *BIT Numer. Math.*, **54** (2014), 937–954. https://doi.org/10.1007/s10543-014-0484-2
13. J. A. Rosenfeld, S. A. Rosenfeld, W. E. Dixon, A mesh-free pseudospectral approach to estimating the fractional Laplacian via radial basis functions, *J. Comput. Phys.*, **390** (2019), 306–322. https://doi.org/10.1016/j.jcp.2019.02.015
14. J. Burkardt, Y. Wu, Y. Zhang, A unified meshfree pseudospectral method for solving both classical and fractional PDEs, *SIAM J. Sci. Comput.*, **43** (2021), A1389–A1411. https://doi.org/10.1137/20M1335959
15. Y. Wu, Y. Zhang, Variable-order fractional laplacian and its accurate and efficient computations with meshfree methods, *J. Sci. Comput.*, **99** (2024), 18. https://doi.org/10.1007/s10915-024-02472-x
16. Z. Hao, Z. Cai, Z. Zhang, Fractional-order dependent radial basis functions meshless methods for the integral fractional laplacian, *Comput. Math. Appl.*, **178** (2025), 197–213. https://doi.org/10.1016/j.camwa.2024.11.027
17. X. G. Zhu, Y. F. Nie, Z. H. Ge, Z. B. Yuan, J. G. Wang, A class of RBFs-based DQ methods for the space-fractional diffusion equations on 3d irregular domains, *Comput. Mech.*, **66** (2020), 221–238. https://doi.org/10.1007/s00466-020-01848-8
18. J. Liu, X. Li, X. Hu, A RBF-based differential quadrature method for solving two-dimensional variable-order time fractional advection-diffusion equation, *J. Comput. Phys.*, **384** (2019), 222–238. https://doi.org/10.1016/j.jcp.2018.12.043
19. B. Fornberg, C. Piret, A stable algorithm for flat radial basis functions on a sphere, *SIAM J. Sci. Comput.*, **30** (2008), 60–80. https://doi.org/10.1137/060671991
20. B. Fornberg, E. Larsson, N. Flyer, Stable computations with Gaussian radial basis functions, *SIAM J. Sci. Comput.*, **33** (2011), 869–892. https://doi.org/10.1137/09076756X
21. E. Hanert, C. Piret, Numerical solution of the space-time fractional diffusion equation: Alternatives to finite differences, in *Proceedings of the 5th Symposium on Fractional Differentiation and its Applications*, 2012.
22. R. Cavoretto, A. De Rossi, M. Donatelli, S. Serra-Capizzano, Spectral analysis and preconditioning techniques for radial basis function collocation matrices, *Numer. Linear Algebra Appl.*, **19** (2012), 31–52. https://doi.org/10.1002/nla.774
23. S. Kumar, C. Piret, Numerical solution of space-time fractional PDEs using RBF-QR and Chebyshev polynomials, *Appl. Numer. Math.*, **143** (2019), 300–315. https://doi.org/10.1016/j.apnum.2019.04.012
24. Q. Zhuang, A. Heryudono, F. Zeng, Z. Zhang, Collocation methods for integral fractional Laplacian and fractional PDEs based on radial basis functions, *Appl. Math. Comput.*, **469** (2024), 128548. https://doi.org/10.1016/j.amc.2024.128548

25. M. Kwaśnicki, Ten equivalent definitions of the fractional Laplace operator, *Fract. Calc. Appl. Anal.*, **20** (2017), 7–51. https://doi.org/10.1515/fca-2017-0002
26. N. S. Landkof, *Foundations of Modern Potential Theory*, Grundlehren der mathematischen Wissenschaftern, Springer, 1972.
27. S. G. Samko, A. A. Kilbas, O. I. Marichev, *Fractional Integrals and Derivatives: Theory and Applications*, Gordon and Breach Science Publishers, Yverdon, 1993.
28. M. Mori, M. Sugihara, The double-exponential transformation in numerical analysis, *J. Comput. Appl. Math.*, **127** (2001), 287–296. https://doi.org/10.1016/S0377-0427(00)00501-X
29. E. J. Fuselier, V. Shankar, G. B. Wright, A high-order radial basis function (RBF) Leray projection method for the solution of the incompressible unsteady Stokes equations, *Comput. Fluids*, **128** (2016), 41–52. https://doi.org/10.1016/j.compfluid.2016.01.009
30. E. J. Fuselier, G. B. Wright, A radial basis function method for computing Helmholtz–Hodge decompositions, *IMA J. Numer. Anal.*, **37** (2017), 774–797. https://doi.org/10.1093/imanum/drw027
31. H. Wendland, *Scattered Data Approximation*, Cambridge University Press, Cambridge, 2005. https://doi.org/10.1017/CBO9780511617539.002
32. T. Gneiting, Strictly and non-strictly positive definite functions on spheres, *Bernoulli*, **19** (2013), 1327–1349. https://doi.org/10.3150/12-BEJSP06
33. C. Foias, O. Manley, R. Rosa, R. Temam, *Navier-Stokes Equations and Turbulence*, Cambridge University Press, 2001. https://doi.org/10.1017/CBO9780511546754
34. H. Helmholtz, Über integrale der hydrodynamischen gleichungen, welche den wirbelbewegungen entsprechen, *J. Reine Angew. Math.*, **55** (1858), 25–55. https://doi.org/10.1515/crll.1858.55.25
35. H. Wendland, Divergence-free kernel methods for approximating the Stokes problem, *SIAM J. Numer. Anal.*, **47** (2009), 3158–3179. https://doi.org/10.1137/080730299
36. A. J. Chorin, J. E. Marsden, *A Mathematical Introduction to Fluid Mechanics*, Springer New York, 1993. https://doi.org/10.1007/978-1-4612-0883-9
37. J. Neustupa, P. Penel, The Navier-Stokes equation with slip boundary conditions, *RIMS Kokyuroku*, **1536** (2007), 46–57.
38. R. J. LeVeque, *Finite Difference Methods for Ordinary and Partial Differential Equations: Steady-State and Time-Dependent Problems*, Society for Industrial and Applied Mathematics, 2007. https://doi.org/10.1137/1.9780898717839
39. I. Akramov, S. Götschel, M. Minion, D. Ruprecht, R. Speck, Spectral deferred correction methods for second-order problems, *SIAM J. Sci. Comput.*, **46** (2024), A1690–A1713. https://doi.org/10.1137/23M1592596
40. J. Wang, X. Chen, J. Chen, A high-precision numerical method based on spectral deferred correction for solving the time-fractional Allen-Cahn equation, *Comput. Math. Appl.*, **180** (2025), 1–27. https://doi.org/10.1016/j.camwa.2024.11.034
41. R. Glowinski, Y. A. Kuznetsov, Distributed Lagrange multipliers based on fictitious domain method for second order elliptic problems, *Comput. Methods Appl. Mech. Eng.*, **196** (2007), 1498–1506. https://doi.org/10.1016/j.cma.2006.05.013

42. C. Garoni, C. Manni, F. Pelosi, H. Speleers, Study and use of spectral symbol properties for isogeometric matrices on trimmed geometries, *Numer. Linear Algebra Appl.*, **32** (2025), e2601. https://doi.org/10.1002/nla.2601

43. M. Mazza, S. Serra-Capizzano, R. L. Sormani, Algebra preconditionings for 2D Riesz distributed-order space-fractional diffusion equations on convex domains, *Numer. Linear Algebra Appl.*, **31** (2024), e2536. https://doi.org/10.1002/nla.2536

44. Y. Wu, Y. Zhang, A universal solution scheme for fractional and classical PDEs, preprint, arXiv:2102.00113.

AIMS Press